ADVANCED MATERIALS
www.advmat.de

Magnesium Nanocomposite Hydrogel Reverses the Pathologies to Enhance Mandible Regeneration

Jiaxin Guo, Hao Yao, Liang Chang, Wangyong Zhu, Yuantao Zhang, Xu Li, Boguang Yang, Bingyang Dai, Xin Chen, Lei Lei, Ziyi Chen, Ye Li, Lizhen Zheng, Weiyang Liu, Wenxue Tong, Yuxiong Su, Ling Qin, and Jiankun Xu**

The healing of bone defects after debridement in medication-related osteonecrosis of the jaw (MRONJ) is a challenging medical condition with impaired angiogenesis, susceptible infection, and pro-inflammatory responses. Magnesium (Mg) nanocomposite hydrogel is developed to specifically tackle multiple factors involved in MRONJ. Mg-oxide nanoparticles tune the gelation kinetics in the reaction between N-hydroxysuccinimide-functionalized hyperbranched poly (ethylene glycol) and proteins. This reaction allows an enhanced mechanical property after instant solidification and, more importantly, also stable gelation in challenging environments such as wet and hemorrhagic conditions. The synthesized hydrogel guides mandible regeneration in MRONJ rats by triggering the formation of type H vessels, activating Osterix+ osteoprogenitor cells, and generating anti-inflammatory microenvironments. Additionally, this approach demonstrates its ability to suppress infection by inhibiting specific pathogens while strengthening stress tolerance in the affected alveolar bone. Furthermore, the enhanced osteogenic properties and feasibility of implantation of the hydrogel are validated in mandible defect and iliac crest defect created in minipigs, respectively. Collectively, this study offers an injectable and innovative bone substitute to enhance mandible defect healing by tackling multiple detrimental pathologies.

1. Introduction

Bone defects frequently result from trauma, tumor resections, infections, and necrotic debridement.[1] Medication-related osteonecrosis of the jaw (MRONJ) attracts great attention in patients receiving medications such as bisphosphonates (BPs),[2] which are commonly used against osteoporosis and bone malignant metastasis.[3] The current treatments of MRONJ include limited debridement, antibiotics, and oral rinses, but there is still a recurrence rate of 11.1% and a delayed healing rate of 29.6%.[4] Multi-predisposing factors such as oral trauma, inhibition of angiogenesis, immune system abnormalities, and infection make mandible regeneration challenging.[5]

Magnesium oxide (MgO), a promising bioactive component, has been approved by the Food and Drug Administration (FDA) for its use as a medication ingredient.[6] The released magnesium ions (Mg^{2+}) participate in multiple

J. Guo, H. Yao, L. Chang, Y. Zhang, X. Li, B. Yang, B. Dai, X. Chen, L. Lei, Z. Chen, Y. Li, L. Zheng, W. Liu, W. Tong, L. Qin, J. Xu
Musculoskeletal Research Laboratory
Department of Orthopedics & Traumatology
Faculty of Medicine
The Chinese University of Hong Kong
Hong Kong SAR 999077, P. R. China
E-mail: lingqin@cuhk.edu.hk; jiankunxu@cuhk.edu.hk

The ORCID identification number(s) for the author(s) of this article can be found under https://doi.org/10.1002/adma.202312920

DOI: 10.1002/adma.202312920

J. Guo, H. Yao, L. Chang, Y. Zhang, X. Li, B. Dai, X. Chen, L. Lei, Z. Chen, Y. Li, L. Zheng, W. Liu, W. Tong, L. Qin, J. Xu
Innovative Orthopedic Biomaterial and Drug Translational Research Laboratory
Li Ka Shing Institute of Health Sciences
Prince of Wales Hospital
The Chinese University of Hong Kong
Hong Kong SAR 999077, P. R. China

W. Zhu
Department of Dental Surgery
The University of Hong Kong-Shenzhen Hospital
Shenzhen, Guangdong 518009, P. R. China

Y. Li
Department of Rehabilitation Sciences
The Hong Kong Polytechnic University
Hong Kong SAR 999077, P. R. China

cellular functions,[7] combat inflammation,[8] and upregulate the genes encoding cytokines in favor of osteogenesis and angiogenesis.[9] Notably, the osteo- and angio-promotive properties of Mg^{2+} in fracture healing and bone defect repair have gained wide recognition.[10] Mg-based implants effectively elevate the calcitonin gene-related peptide (CGRP) synthesis and enhance the angiogenesis process in BPs-impaired fracture healing and MRONJ.[11] Moreover, Mg^{2+} suppressed M1 macrophages as presenting with a decrease in proinflammatory factors such as tumor necrosis factor-α (TNF-α), interleukin (IL)-1β, and IL-6, thus we synthesized MgO nanoparticle (NP) bandages to facilitate bone regeneration by inducing a desirable immune microenvironment.[12] Last but not least, MgO has broad-spectrum antibacterial properties and non-resistance to antibiotics,[13] and therefore may improve the healing of MRONJ which usually faces a higher infection risk.[14]

Hydrogels show potential in periodontal and maxillofacial bone tissue engineering attributed to their excellent plasticity and efficient degradation into surrounding tissues.[15] However, the effectiveness of hydrogel can be compromised in certain situations, such as slow curing, insufficient adhesion, and inability to crosslink in hemorrhage.[16] Amidation reaction takes place quickly under alkaline conditions via the process where the hydrogen atom on an amino group is replaced by amide groups.[17] N-hydroxysuccinimide (NHS)-functionalized polymer can bind bioactive proteins and peptides via amidation reaction.[18] MgO reacts with body fluids and produces hydroxide, which continuously hydrolyses into Mg^{2+} and hydroxide ions (OH^-) in the presence of chloride.[19] So, it is anticipated that MgO might retard the decrease of pH during the amidation reaction, thereby preserving the nucleophilicity of -NH_2 on proteins, and shortening the gelation time to achieve injectability.[20] Additionally, the excess NHS-esters in the precursor not only enables the formation of covalent bonding with freely exposed amino groups in vivo,[21] but also interacts with plasma proteins, resulting in rapid crosslinking even under hemorrhage conditions.

To provide a biomaterial for effectively repairing irregular and multifactor-induced mandible defects, we developed a MgO nanocomposite hydrogel, investigated its effects on bone regeneration in rats with MRONJ, and demonstrated its promising applications in mandible defects using minipig models.

2. Results

2.1. Design and Preparation of PBM Hydrogels for Mandible Regeneration

We fabricated the hydrogels via amidation reaction with adjustable gelation kinetic. In this process, NHS groups were used to functionalize the hyperbranched poly (ethylene glycol) (PEG), which was covalently linked to bovine serum albumin (BSA) and amino-collagen-mimicking short peptide arginylglycylaspartic acid (a-RGD). By mixing all of the precursors with MgO NPs, we obtained the PEG-BSA/a-RGD@MgO NPs (PBM) hydrogels (**Figure 1A**). PBR hydrogels were prepared using the hydrogel precursors without MgO NPs, serving as the material control.

A series of hydrogels were prepared using different precursors with varying pH levels (7.4 and 8.6) or concentrations of MgO NPs (ranging from 5 to 20 mg mL^{-1}). Scanning electron microscopy (SEM) showed NPs randomly attached to the interconnected network of the hydrogels, which revealed the concentration-dependent effect of MgO NPs on the network density of the hydrogels (Figure 1B). The energy dispersive spectrum (EDS) analysis pattern illustrated the proportional distribution of C, N, O, and Mg that confirmed the loading of MgO NPs (Figure S1, Supporting Information). As the NPs became more involved, the pH of the precursor solution elevated, resulting in the formation of more robust amide bonds (Figure 1B). The Fourier-transform infrared spectroscopy (FTIR) analysis revealed distinct peaks of absorbance indicative of amide bonds. Notably, the increased presence of MgO NPs in PBM(5) and PBM(10) nanocomposite hydrogels led to more amide bond formation in comparison to the PBR hydrogel (Figure S2, Supporting Information). As a result, the network distances were adjusted by the concentration of MgO NPs, ranging from 29.1 ± 3.2 μm (20 mg mL^{-1} MgO NPs) to 72.5±12.6 μm (5 mg mL^{-1} MgO NPs) (Figure S3, Supporting Information).

In line with our hypothesis, we attempted to precisely regulate the gelation time in a dose-dependent manner. The precursor solution could not gel within half an hour at pH 7.4, but the process presented rapid gelation (≈1 min) with the presence of 10 mg mL^{-1} MgO NPs. Further increasing the content of MgO NPs (≥ 20 mg mL^{-1} MgO NPs) resulted in ultrafast gelation (in 10–25 s) (Figure 1C). Quantitative results showed that the gelation time ranged from 804.0 to 9.6 s, depending on the concentration of MgO NPs (ranging from 1 mg/mL to 30 mg/mL) at room temperature (Figure 1D).

2.2. Robust Adhesion and Unaffected Function in Hemorrhage

The ability to control gelation time enabled the hydrogels to be injected while offering adaptability in shaping. We successfully achieved various patterns, such as the "CUHK" pattern through injection (Figure S4, Supporting Information). Furthermore, the mixed precursors transformed into hydrogels even underwater and tightly adhered to the glass plate with water surrounding them (Figure S4, Supporting Information). The extensive adhesion was further confirmed through experiments conducted on either soft or hard tissues, including gingival tissue, mandible, and femur. SEM images illustrated the intimate integration of the hydrogels with the adjacent tissue at the microscale (Figure S5, Supporting Information).

Additionally, hemorrhage in bone defect areas posed challenges during the implantation surgery of bone substitutes. Injectable hydrogels, for instance, might lose their function due to the liquid precursors being diluted or diffused away from the bleeding site without proper gelation.[22] However, our PBR and

L. Zheng
Centre for Regenerative Medicine and Health
Hong Kong Institute of Science and Innovation
Chinese Academy of Sciences
Hong Kong SAR 999077, P. R. China
Y. Su
Division of Oral and Maxillofacial Surgery
Faculty of Dentistry
The University of Hong Kong
Hong Kong SAR 999077, P. R. China

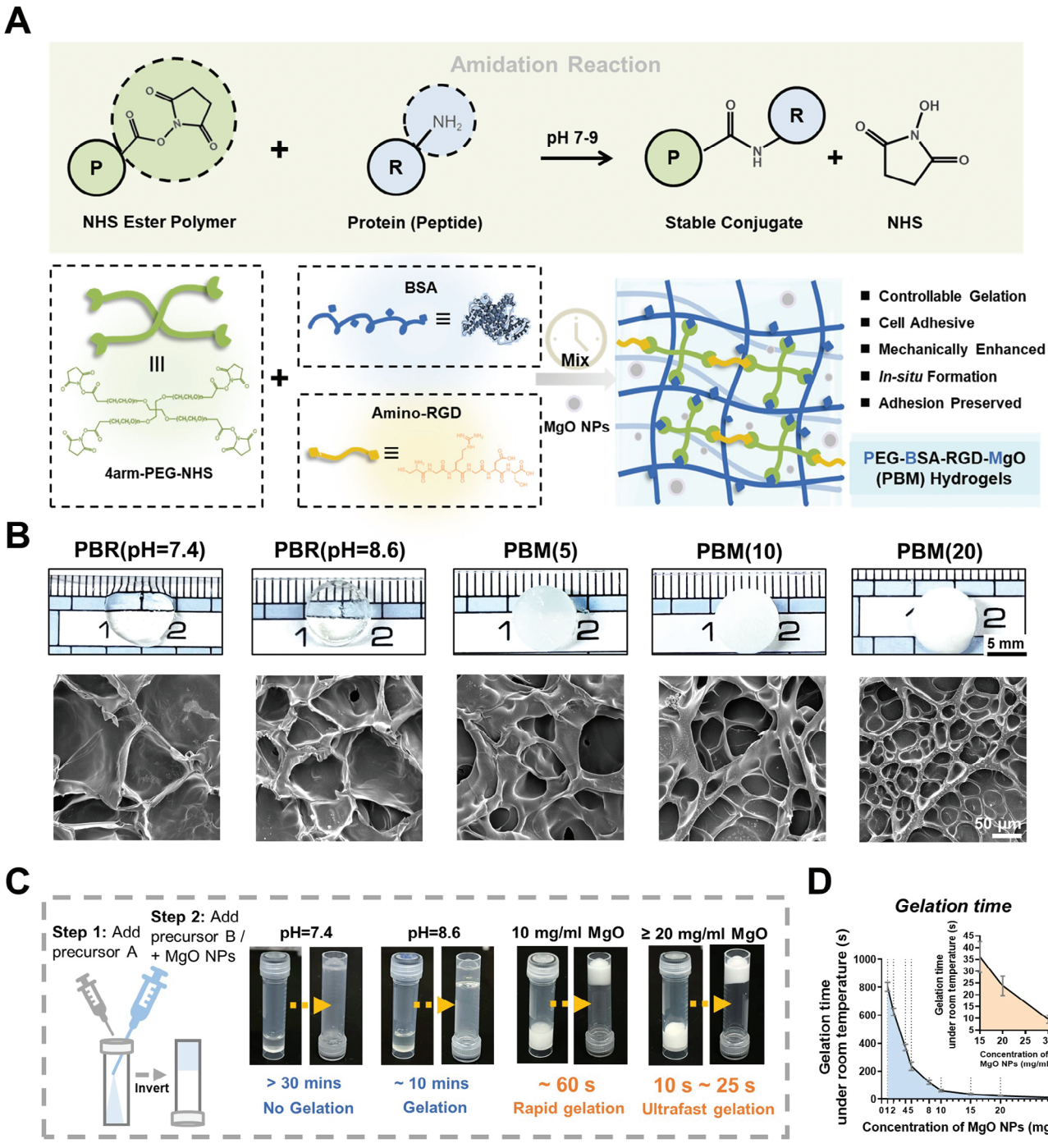

Figure 1. Design, fabrication, and controlled gelation of PBM hydrogels. A) Schematic illustration of crosslinking mechanism and design of PBM hydrogel. B) The gross-view of the hydrogels and the internal microstructure observed by SEM. C) Photographs and D) quantification of the controllable gelation behavior tuned by MgO NPs ($n = 5$). PBR(pH = m) hydrogels were defined as hydrogels formed under a pH = m condition of hydrogel precursor B. PBM(n) hydrogels referred to hydrogels formed with the addition of n mg/mL MgO NPs in precursor B.

PBM hydrogels were specifically designed to effectively function even in the presence of blood. This was achieved through the rapid crosslinking between the abundant proteins in the blood and the hydrogel precursors, with the presence of MgO NPs further enhancing and expediting this process (**Figure** 2A). The gelation times of hydrogels were examined by using heparinized whole blood extracted from rats. A mixture of precursor solutions and blood in a vial induced rapid gelation, particularly within 2 min, PBM(5), PBM(10), and PBM(20) hydrogels adhered firmly to the bottom of the vial after inversion of the vial (Figure 2B). In contrast, a small amount of blood flowed down from the blood-PBR gel mixture after vial inversion within

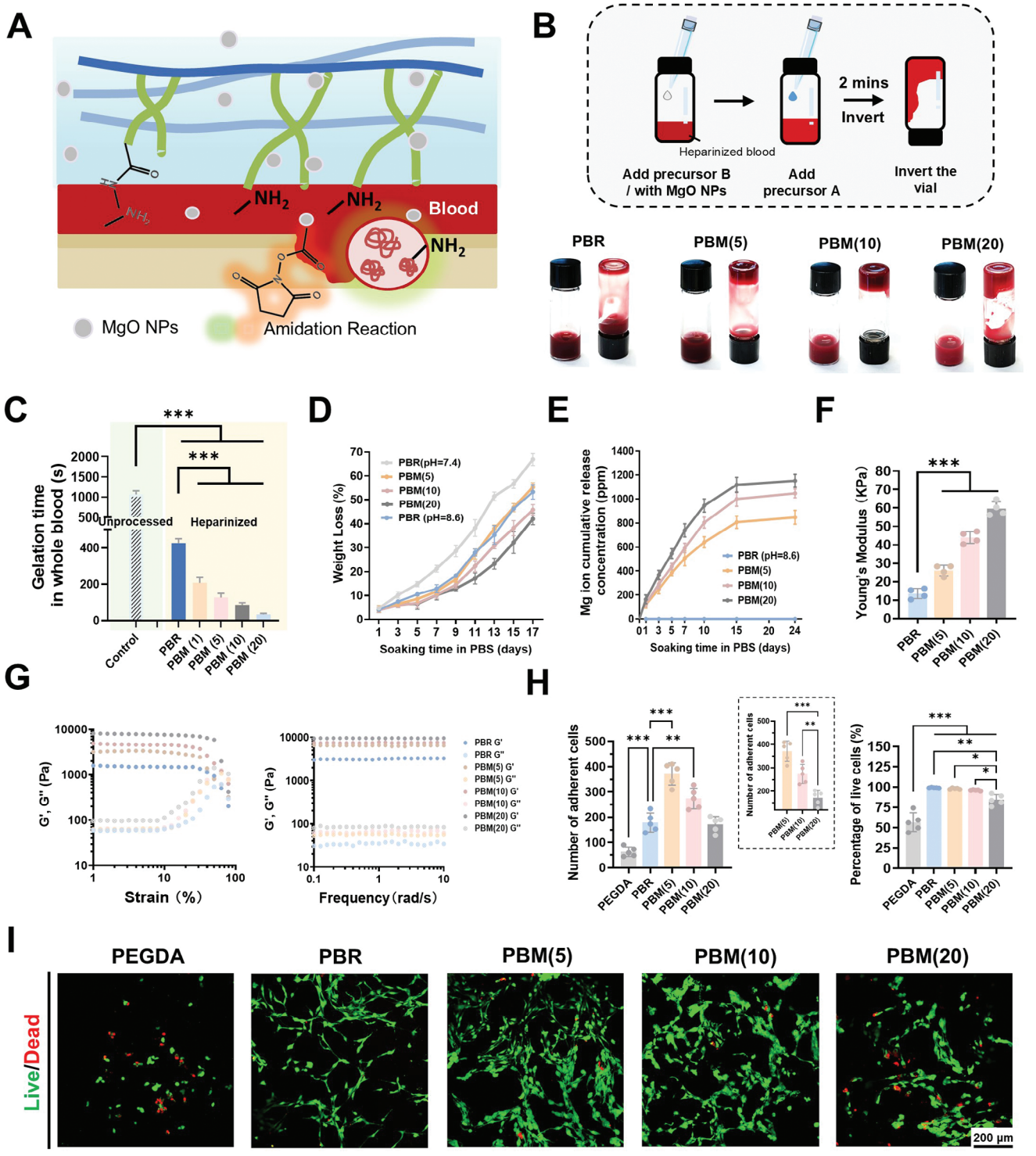

Figure 2. Optimized physiochemical properties and cytocompatibility of hydrogels by MgO NPs. A) The illustration depicted the design of PBM hydrogels functioning in hemorrhage. B) Photographs and C) quantification of the gelation behaviors of hydrogels within blood using the vial tilting method ($n = 3$). D) Weight loss and E) cumulative concentration of Mg^{2+} released from hydrogels during in vitro degradation tests ($n = 3$). F) Young's modulus ($n = 4$). G) Storage modulus (G′) and loss modulus (G′′) through strain and frequency sweep tests. H) Quantitative analysis of cell adhesion and viability ($n = 5$). I) Live (green) /dead (red) staining of MMSCs cultured with hydrogel systems. *$p < 0.05$, **$p < 0.01$, and ***$p < 0.001$, by one-way ANOVA with Tukey's *post hoc* test.

2 min, and gelation of the mixture occurred at ≈7 min. Nevertheless, PBR and PBM hydrogels significantly shortened the in vitro clotting time compared to the natural blood coagulation process, which took over 15 min, and this process was not dependent on the self-coagulation capability of blood (Figure 2C). This greatly facilitated their implantation into bone defects accompanied by bleeding. Subsequently, the in vivo imaging system detected the retention of the PBM hydrogel at the targeted site. Over 28 days, the average fluorescence intensity gradually decreased from 4.821e^9 p/s/cm^2/sr (Day 0) to 1.713e^9 p/s/cm^2/sr (Day 28), accompanied by its degradation in vivo (Figure S6, Supporting Information).

2.3. Optimized Physiochemical Properties and Cytocompatibility of Hydrogels by MgO NPs

After successfully fabricating the PBM hydrogels, we adjusted the content of MgO NPs to investigate the physiochemical properties and optimized the hydrogel system for bone regeneration. First, the in vitro weight loss of hydrogels was examined over 17 days. The presence of MgO NPs slightly decreased the degradation rate due to the denser crosslinks, resulting in prolonged Mg^{2+} release. Over the tested period, the PBM(20) lost 42.00% ± 2.47% weight, while the PBR hydrogels experienced a weight loss of 66.87% ± 2.60% (Figure 2D). This significant difference suggested that the incorporation of NPs resulted in a stronger structure and more stable crosslinks, which were absent in the individual polymers. During the degradation, the MgO NPs reacted with buffer, leading to the gradual release of Mg^{2+} from PBM hydrogels for over 4 weeks (Figure 2E).

MgO NPs also significantly augmented the compressibility of hydrogels. The Young's modulus of the hydrogels increased from 13.59 ± 2.74 KPa to 59.66 ± 3.86 KPa in a concentration-dependent manner (Figure 2F). Rheological characterization showed that the storage modulus (G') was consistently greater than the loss modulus (G″) across all groups of hydrogels, indicating the robustness of the internal structure. During the strain sweep test, the intersection positions of G′ and G″ in different groups remained similar, suggesting the inclusion of MgO NPs did not significantly alter the toughness of the hydrogels (Figure 2G).

Subsequently, the mandible-derived mesenchymal stem cells (MMSCs) were co-cultured with hydrogel systems to investigate cytocompatibility.[23] Modifying hydrogel with a-RGD peptides enhanced the cell adhesive property of PBR and PBM hydrogels, as evidenced by cell viability exceeding 95% in the PBR, PBM(5), and PBM(10) groups (Figure 2H). MgO NPs could change the topography and roughness of the surface, meanwhile further improving cell adhesion. MgO NPs significantly increased cell proliferation on the surface of PBM(5) and PBM(10) hydrogels after 3 days' culture compared to the PBR group, with respective 2.08-fold and 1.53-fold enhancement (Figure 2H,I). Moreover, it was observed that concentrations of 5 and 10 mg mL^{-1} MgO NPs did not significantly affect the cell infiltration into the hydrogel (Figure S7, Supporting Information). However, overloading of MgO NPs (>20 mg mL^{-1}) inhibited cell proliferation and infiltration, which was caused by the over-alkaline environment and the reduction of internal sizes (Figure S7, Supporting Information).

2.4. Pro-Osteogenic and Angiogenic Effects of PBM Hydrogels In Vitro

The effects of Mg^{2+} on osteogenic differentiation varied with concentrations.[12a] Compared to the normal medium containing 0.8 mM Mg^{2+}, bone marrow-derived mesenchymal stem cells (BMSCs) exposed to a high concentration of Mg^{2+} (20 mM) exhibited a significant increase in the late apoptotic or necrotic population.[24] Thus, PBM(5) and PBM(10) hydrogels were chosen for differentiation assay referring to cytocompatibility results. The expressions of osteogenic genes (*Alp*, *Osterix*, *Runx2*, *Bmp-2*, and *Ocn*) were significantly increased in the MMSCs treated with the extracts of PBM hydrogels. Specifically, expression levels of *Alp*, *Osterix*, and *Runx2* were significantly increased at the early stage, while with longer exposure, the *Bmp-2* and *Ocn* levels in the PBM(10) group were ≈5 folds and 3 folds higher than those of the Control (Ctrl) group, respectively (**Figure** 3A). In 3D co-culture systems, cells seeded in PBM hydrogels exhibited significantly higher immunofluorescence (IF) intensities of Ocn (Figure 3B,C). The extracts of PBM hydrogels also increased alkaline phosphatase (ALP) activity and calcium-rich deposits on 5 days and 21 days post-induction, respectively (Figure 3D).

Since the initiation of ossification was closely associated with the presence of blood vessels, we investigated the angiogenic differentiation of endothelial cells in response to different hydrogel treatments. In vitro experiments showed the migration of the human umbilical vein cell line (EA.hy926) was significantly improved by the extracts of PBM(5) and PBM(10) hydrogel compared with PBR (Figure 3E,F). Of note, the PBM(10) hydrogel group presented with more capillary-like structures, as indicated by a 2.24-fold increase in branch number and a 2.48-fold increase in branch length compared to the Ctrl group (Figure 3G,H). Altogether, the above results highlighted the potent osteo- and angio-promotive properties of PBM hydrogels in vitro.

2.5. PBM Hydrogel Augmented Bone Regeneration in Mandible Osteonecrosis

Regenerating the mandible is challenging in MRONJ owing to the complicated pathologies. Zoledronate (ZOL)-treated rats developed mandibular osteonecrosis and were susceptible to infection in the extraction socket after tooth extraction, consistent with MRONJ lesions as reported in humans.[25] To establish a rat MRONJ model, we followed the established protocols.[11b,26] Rats were administered with a high dose of ZOL intraperitoneally injection at 0.3 mg k^{-1}g/week for 12 consecutive weeks, followed by teeth extraction to simulate the most common trigger of MRONJ in patients. Subsequently, a mandible defect was created around the tooth extraction site. The Sham group without ZOL treatment also underwent dental procedures and defect creation (Figure S8, Supporting Information).

At 8 weeks post-operation, in the ZOL-pretreated group, MRONJ-like lesions of large open wounds were present, with exposure of necrotic bone in extraction sites. In contrast, the Sham group exhibited clean and complete oral socket healing (Figure S8, Supporting Information). Histologically, the ZOL-pretreated group displayed a significantly higher percentage and

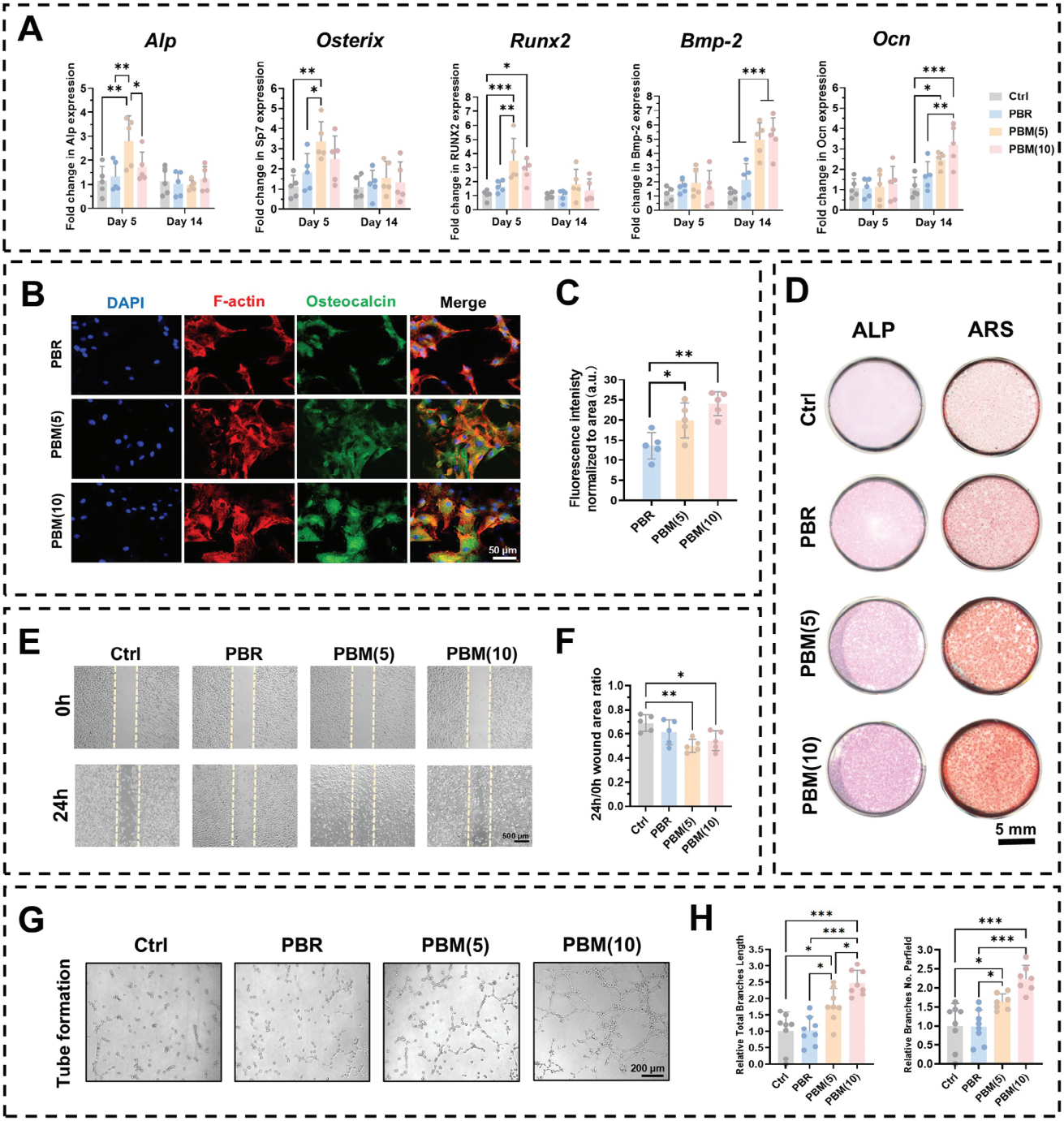

Figure 3. Osteo- and angio-promotive effects of PBM hydrogels in vitro. A) Quantitative osteogenic related-gene expression of MMSCs determined by qPCR on Day 5 and 14 ($n = 5$). B, C) Representative images and quantification of fluorescent intensity ($n = 5$). D) ALP and alizarin red S (ARS) staining. E, F) Migration (scratch test; $n = 5$) and (G-H) tube formation assay ($n = 7$-8). *$p < 0.05$, **$p < 0.01$, and ***$p < 0.001$, by two-way (A) or one-way (C, F, H) ANOVA with Tukey's *post hoc* test.

number of empty lacunae at the defect margin, indicating a greater presence of histological signs indicative of osteonecrosis at 8 weeks (Figure S9, Supporting Information). These findings confirmed the successful establishment of the rat MRONJ model (**Figure** 4A). Subsequently, we implanted PBR and PBM hydrogels into MRONJ rats with mandible defects, while the Ctrl group received no hydrogel implantation under the MRONJ condition (Figure 4B). During the follow-up, the maxillofacial operation did not affect the body weight of the animals (Figure S10, Supporting Information).

According to the radiographs, the PBM group displayed stronger periosteal reaction and bone deposition as compared to

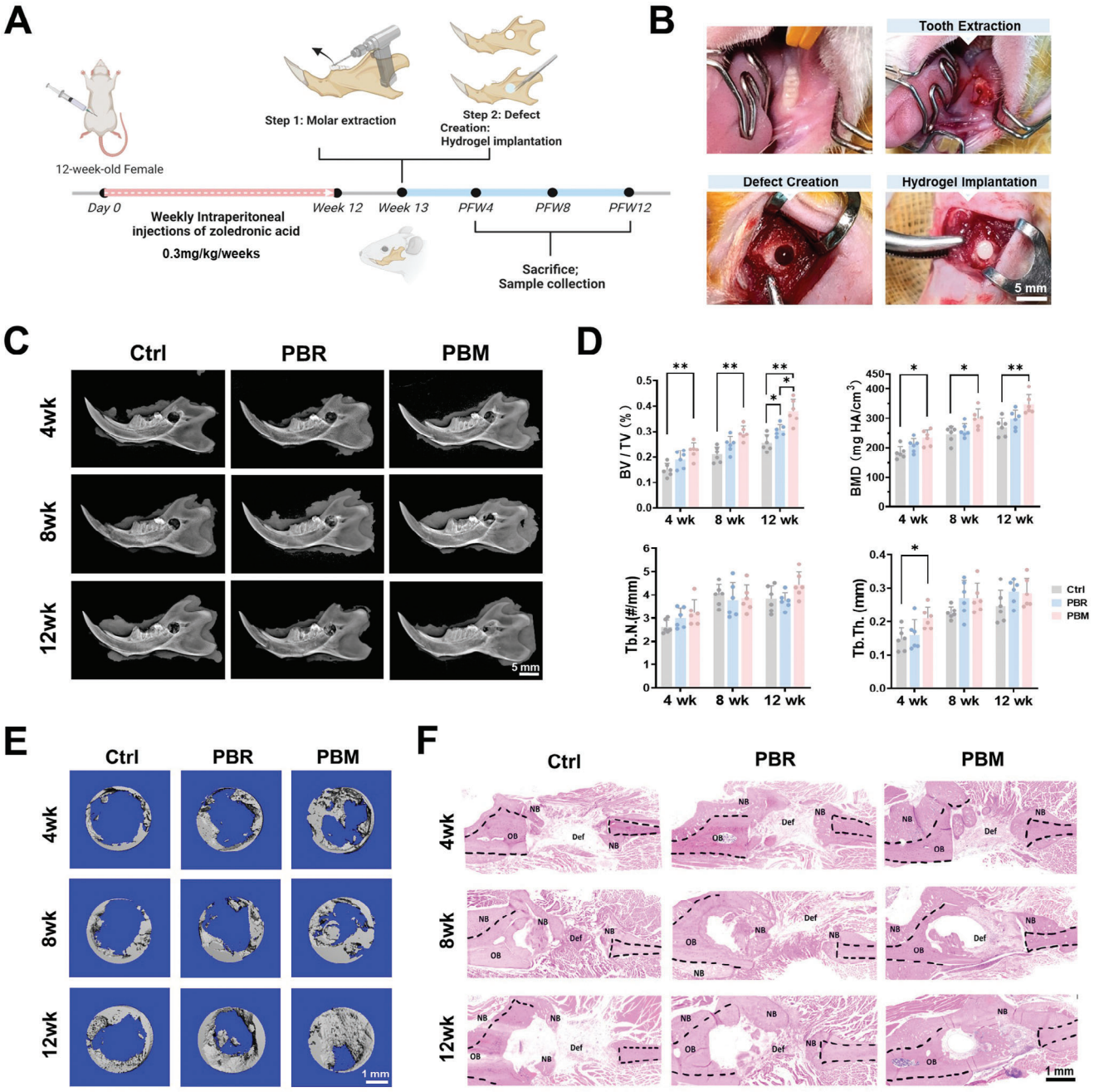

Figure 4. PBM hydrogels augmented mandible bone regeneration in MRONJ. A, B) Schematic diagram and surgical photographs of MRONJ model establishment, and surgical procedures involving dental extraction, mandible defect creation, and implant implantation. C) Representative radiographs, D) Quantitative micro-CT measurements ($n = 6$), E) 3D reconstructed images of mandible defects at 4, 8, and 12 weeks. F) Representative H&E staining of mandible defect, showing the histological morphology of newly-formed bone (NB), old bone (OB), and the defect (Def). $^{*}p < 0.05$ and $^{**}p < 0.01$, by two-way ANOVA with Tukey's *post hoc* test.

the Ctrl and PBR group, with the regenerated bone formed covering the defect at 12 weeks (Figure 4C).

In particular, the quantitative analysis of newly-formed bone volume fraction (BV/TV) revealed the highest values in the PBM group, which were 1.50-, 1.40-, and 1.48- times higher than that of the Ctrl group at 4, 8, and 12 weeks, respectively. Besides, PBM hydrogel significantly enhanced the bone mineral density (BMD) of the newly-formed mandible, while there was no significant difference in BMD between the PBR group and the Ctrl group (Figure 4D,E). Hematoxylin and eosin (H&E) staining of major organs showed no significant morphological changes at 4 weeks, indicating the satisfactory safety profile of the nanocomposite hydrogel (Figure S11, Supporting Information). Histological staining exhibited that newly-regenerated trabecular-like bone

tissue originated from the periosteum and continuously formed toward the center of the defect site in all groups. We observed limited mandible regeneration in pathological conditions in the Ctrl group without scaffold implantation (Figure 4F). On the other hand, the PBR and PBM hydrogels stimulated intramembranous ossification, characterized by the thicker newly-formed bone, especially at 4 weeks. Over time following implantation, the regenerated bone gradually flattened and matured (Figure S12, Supporting Information). Notably, the PBM hydrogels induced substantial amounts of intramembranous bone formation at the bone defect site and completely bridged the healing interface at 12 weeks.

2.6. Promoted Angiogenesis and Stem Cell Recruitment by PBM Hydrogels

Immunohistochemistry (IHC) staining was performed to evaluate the osteogenesis-related proteins during the healing process. Osterix was expressed in osteoblasts, which played a crucial role in intramembranous osteogenesis. Histologically, the Osterix+ cells were assembled at the margins of the bone defect and scattered surrounding the newly-formed bone (**Figure 5**A). The expression of Osterix significantly increased in the PBM group than that in the Ctrl and PBR groups at both 4 and 8 weeks, indicating a more active guided bone regeneration (GBR) (Figure 5B). Furthermore, the expression of Ocn peaked at 8 weeks in all groups, which regulated bone mineralization and calcium ion homeostasis during bone formation. The Ocn+ cells were localized in the newly formed bone tissue. In the PBM group, the expression of Ocn was significantly higher, as compared to the PBR and Ctrl groups at 8 weeks (Figure 5B,C).

To investigate if angiogenesis was facilitated by PBM hydrogels, we performed IF staining of type H vessels, which were characterized by high expression of Endomucin (Emcn) and CD31 concurrently. Previous studies indicated that these specialized blood vessels were closely associated with osteogenic activity. They nurtured the perivascular osteoprogenitor cells and influenced the proliferation and differentiation of cells in a paracrine manner, thereby creating a suitable microenvironment to facilitate new bone formation.[27] As expected, the CD31+ Emcn+ Type H vessels were significantly increased in the PBM group at 4 weeks (Figure 5D,E). Besides, we observed that Type H vessels were surrounded by Osterix+ osteoprogenitors. Notably, the PBM group exhibited a dramatically higher abundance of Emcn+ vessels and associated Osterix+ osteoprogenitor cells in the regenerated bone compared to that of the Ctrl and PBR groups (Figure 5F,G). In addition, the quantitative micro-CT angiography analysis of samples from 8 weeks revealed significant increases in both the volume fraction and number of vessels in the defect site of the PBM group (Figure 5H).

Excluding the non-osteogenic tissues from interfering with bone regeneration is a key principle of GBR.[28] We quantified the fibrous tissue using antibodies targeting collagen type III alpha 1 (Col3a1) and fibronectin (Fn). The results showed the implantation of the PBM hydrogel effectively protected bone formation by preventing the infiltration and proliferation of fibrous tissue into the defect site at 4 weeks (Figure S13, Supporting Information). The PBM hydrogel could act as a physical and bioactive barrier to prevent the ingrowth of soft tissue.

In addition, since periostin (Postn) has been identified as a crucial molecule in modulating periosteal skeletal stem cells-mediated bone regeneration, Postn expression was detected by IF staining in the periosteum at the periphery of the ossified callus at 4 weeks. As a result, Postn expression was upregulated in response to injury in all groups. Notably, we found that the number of stem cells labeled by the CD105 significantly increased in the Postn-positive region in the PBM group (Figure 5I,J). These findings indicated that the PBM hydrogel enhanced the enrichment of stem cells within the periosteum. The increase of the stem cells derived from the periosteum contributed to massive bone formation.

2.7. PBM Hydrogels Upregulated Angiogenesis and Downregulated Inflammation During the Healing of Mandible Defect

To gain insights into the potential mechanisms underlying the enhanced mandible regeneration promoted by PBM hydrogels, we conducted bulk-RNA sequencing to identify the differentially expressed genes (DEGs) in mandible defects at 4 weeks. The samples were stratified into 3 clusters by a hierarchical analysis of the selected DEGs (**Figure 6**A). Volcano plots showed 666 DEGs between the Ctrl and PBM groups, while 304 DEGs were identified between the PBR and PBM groups (Figure 6B).

Gene Ontology (GO) enrichment analyses were conducted to assess the functions of these DEGs in biological processes. In comparison to the Ctrl group, several processes were found to be significantly upregulated in the PBM Group, including biomineral tissue development, endothelium development, and regulation of interleukin (IL)-4 and IL-10 production (Figure 6C). Notably, PBM hydrogels activated the CXCL12/CXCR4 axis, which was reported to play a role in bone homeostasis, and fracture healing, and tentatively applied in tissue engineering, through its homing effects on immune cells and osteogenic precursor cells.[29] Conversely, processes such as keratinocyte differentiation, chronic inflammatory response, negative regulation of blood vessel endothelial cell proliferation, and transforming growth factor-β production were downregulated by PBM hydrogels (Figure 6D). Given the reported cases of MRONJ and the observed massive infiltration of inflammatory cells in clinical symptoms, PBM hydrogels exhibited the ability specifically aimed at addressing the immune responses and inflammation associated with MRONJ.

Furthermore, compared to the PBR hydrogels, PBM hydrogels demonstrated significant enhancements in bone maturation, blood vessel formation, neuron differentiation, and skeletal muscle tissue regeneration (Figure 6E), elevating the genes expression, including *Fgfr1*, *Plxnb1*, *Tcf12*, and *Dysf*. In contrast, PBM hydrogel downregulated the inflammatory response (like IL-1 medicated signaling pathway), keratinization, and cytokine-medicated signaling pathway (Figure 6F). PBM hydrogels surpassed the capabilities of PBR hydrogels by creating an alkaline environment and facilitating sustained release of Mg^{2+} during the early stages of healing. The MgO NPs and their degraded products not only reduced inflammation but also activated

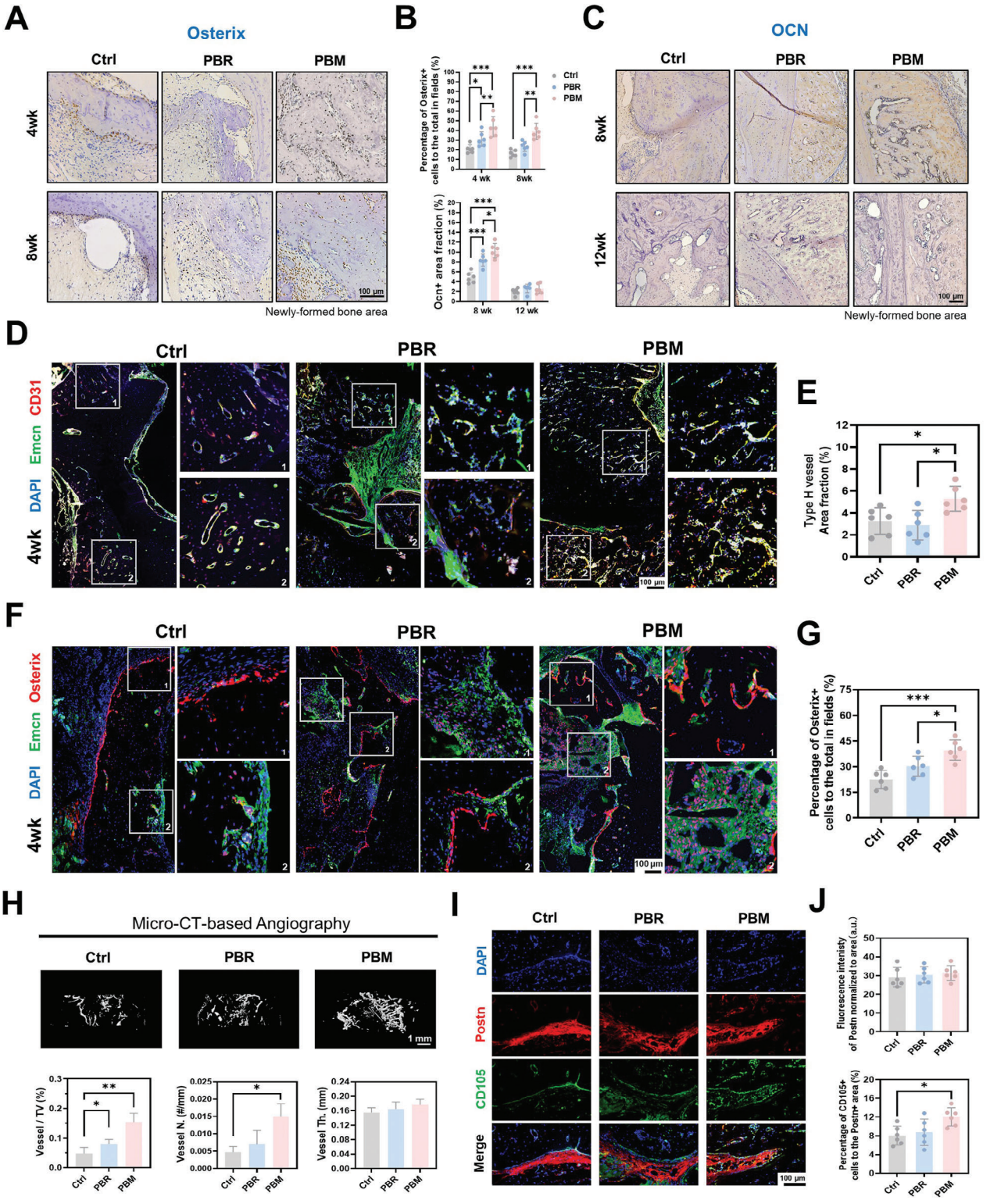

Figure 5. PBM hydrogel enhanced angiogenesis and stem cell recruitment in mandible regeneration. A–C) IHC staining and quantitative analysis on the expression of Osterix and Ocn ($n = 6$). D, E) IF staining and quantification of type H vessels (CD31+ Emcn+) at 4 weeks ($n = 6$). F, G) IF staining and quantification of Osterix+ osteoprogenitor cells and Ecmn+ vessels at 4 weeks ($n = 6$). H) Representative 3D reconstructed images of micro-CT angiography, and quantification of vessel volume fraction (Vessel V/TV), vessel number (Vessel.N), and vessel thickness (Vessel.Th) through different treatments at 8 weeks ($n = 3$). I, J) IF staining and quantification of Postn+ area and active CD105+ stem cells in the newly-formed bone at 4 weeks ($n = 6$). $^*p < 0.05$, $^{**}p < 0.01$, and $^{***}p < 0.001$, by two-way (B) or one-way (E, G, H, J) ANOVA with Tukey's *post hoc* test.

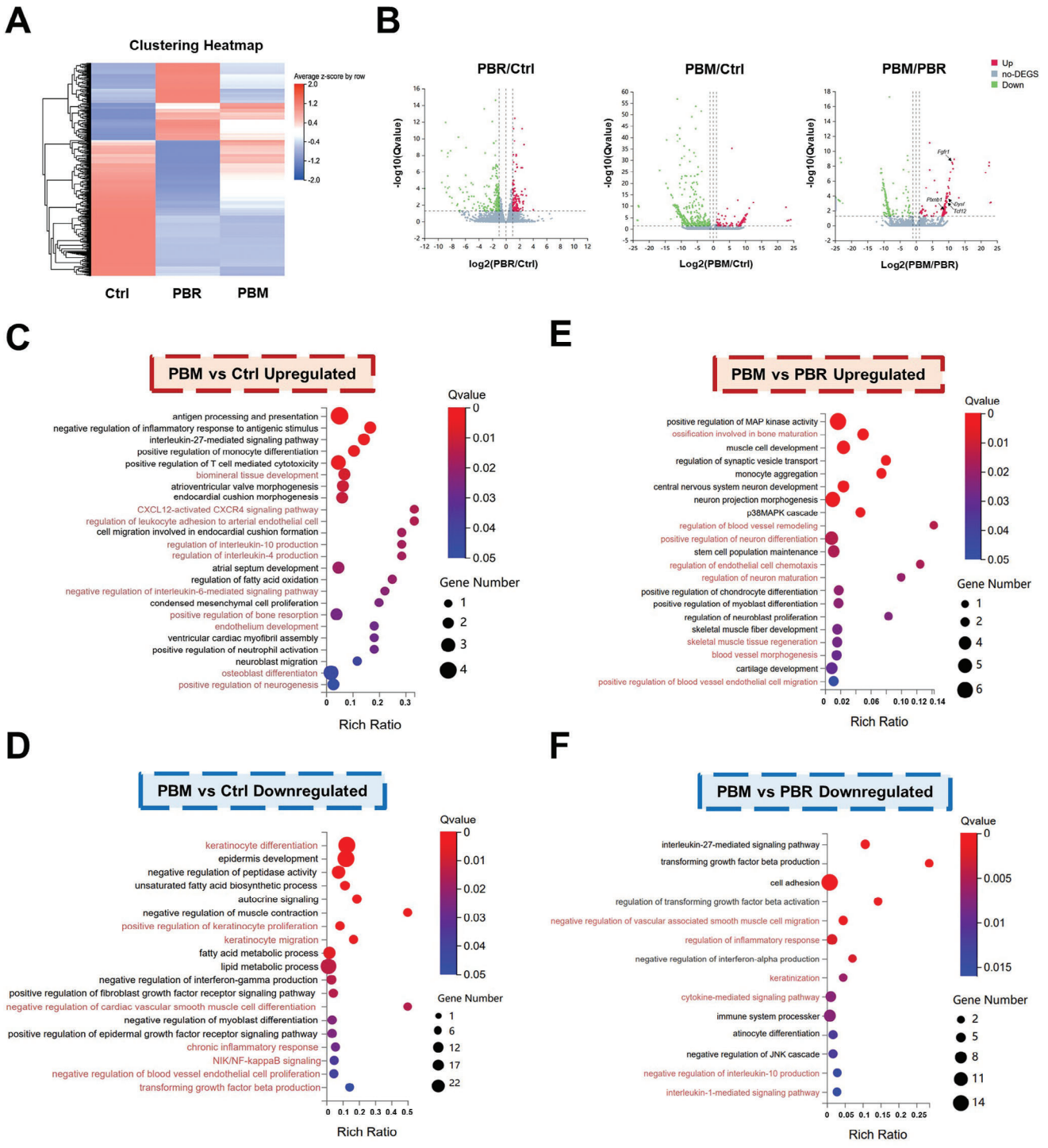

Figure 6. Underlying mechanisms uncovered by bulk-RNA sequencing. A) Unsupervised hierarchical clustering of transcriptomes in different groups. B) Volcano plots of the upregulated and downregulated genes between Ctrl, PBR, and PBM group (False discovery rate < 0.05 and Fold change > 2). Gene ontology biological process enrichment of genes C) upregulated and D) downregulated in PBM group than Ctrl group; Gene ontology biological process enrichment of genes E) upregulated and F) downregulated in PBM than PBR group (Q value < 0.05).

angiogenesis and neurogenesis, thereby leading to more effective bone formation and advanced remodeling processes in MRONJ.

2.8. Local Microbial Changes Following the Use of PBM Hydrogel

The alveolar bone in the mandible is particularly susceptible to pathogens present in oral mucosal lesions, as it is only separated by a thin and vulnerable layer of periosteum and epithelium.[30] Such a unique nature tends to aggravate MRONJ, which arouses our interest in investigating the local microbial changes following the application of PBM hydrogels. Therefore, we collected samples of microorganisms from the defect areas and performed 16S rDNA sequencing analysis (**Figure** 7A). The Sham group, which was in the normal state without MRONJ induction, served as the control. The Venn diagram depicted the amplicon sequence variants (ASVs) identified in the samples (Figure 7B).

Under MRONJ, the local microbial displayed increased complexity and a wider range of composition and structure. However, the microbial community after PBM hydrogel treatment was more stable and uniform, as shown by the PCoA and NMDS plots (Figure 7C). We analyzed the expression of dominant bacterial species and determined their proportions at the Phylum level. Our findings revealed a higher prevalence of *Firmicutes*, *Fusobacteriota*, and *Bacteroidota* in the MRONJ group (Figure 7D). The correspondence between different treatment groups and bacteria species was analyzed, uncovering that the PBM hydrogel effectively reduced the abundance of *Bacteroidota* (Figure S14, Supporting Information). To delve into the Genus level, it was observed that PBM hydrogel had a notable inhibitory effect on *Bacteroides, Proteus*, and *Barnesiella*, reversing the promotive effect from BPs. *Bacteroides* was associated with diseased periodontal tissue, inflammation, and measures of distress in clinical findings.[31] Furthermore, the use of PBM hydrogel aided in restoring the population level of *Rothia* and *Lactobacillus* (Figure 7E), which were known colonizers of the human oral cavity.[32]

Based on species prediction, a significant increase in the abundance of Gram-positive bacteria and anaerobic bacteria in MRONJ was observed, accompanied by a decrease in biofilm formation and stress tolerance. The dysbiosis in oral microbiota might create an environment for the colonization of opportunistic pathogens.[33] PBM hydrogel partially restored the Gram-negative bacterial populations and significantly diminished the abundance of anaerobic bacteria upregulated in MRONJ. Additionally, the hydrogel improved the stress tolerance of the bacterial community against external disruptions (Figure 7F). These findings confirm that PBM hydrogel can regulate local microbial composition toward a normal state, particularly in cases characterized by high-risk dysbiosis and alterations in oral microbial composition associated with MRONJ.

2.9. Promising Application of PBM Hydrogels for Bone Defect Filling and Healing in Minipigs

We further illustrated the convenience of PBM hydrogel implantation by injecting it into the mandible and iliac crest defects in minipig models. Video (Movie S1,S2, Supporting Information) showcased the surgical procedures, where the hydrogel precursors were thoroughly mixed using a three-way valve for preparation, and then were conveniently injected into the defect sites. Within seconds, the PBM hydrogel underwent rapid in situ solidification, forming a tight adherence to the surrounding tissues in irregular defects to support regeneration (**Figure** 8A,B).

The therapeutic efficacy of PBM hydrogel was further evaluated by the mandible defect model in the minipig. Three artificial mandible defects were created on each side of the mandibles. PBM hydrogel was administered to the defect areas, while the Ctrl group did not receive hydrogel treatment. No instances of weight loss or ingestion problems were observed during experiments. In vivo, CT scans were performed at 2 and 4 weeks. The index of new bone formation in the PBM group, defined as the average distances within the defect, was significantly smaller than that of the Ctrl group at 4 weeks (Figure 8C,D). The minipig samples were harvested at 8 weeks. Radiographs displayed the obvious uncovered defects in the Ctrl group, whereas the PBM group showed almost full coverage of newly-formed bone. Based on the Micro-CT quantitative analysis, the PBM group exhibited significantly higher newly-formed BV/TV and reduced trabecular separation (Tb.Sp.), indicating the enhanced bone regeneration facilitated by hydrogel scaffolds (Figure S15, Supporting Information). H&E staining revealed the infiltration of fibrous tissue into the bony defects in the Ctrl group, while the PBM hydrogel demonstrated a protective effect by preventing fibrous tissue intrusion and promoting the development of new bone in the defect area (Figure 8E). Furthermore, the regenerated bone in the PBM group harbored more abundant Type H vessels and a significant enrichment of Osterix+ osteoprogenitor cells compared to the Ctrl group (Figure 8E,F). Taken together, the injectable PBM hydrogel showed promise for clinical translation, demonstrating convenient surgical application and effective promotion of mandibular bone regeneration in large animal models.

3. Discussion and Conclusion

MRONJ is a widely recognized pathological entity that poses healing challenges and unsatisfied recovery.[34] The overall incidence of MRONJ varies greatly across studies due to the complicated related risk factors. Reported rates range from 0.01% following oral use of low-dose BPs to 14.4% in patients receiving high-dose intravenous medication.[35] Among patients with a cancer diagnosis treated with ZOL, cumulative incidence is reported to range from 0.7% to 6.7%.[36] The pathogenesis of MRONJ remains controversial. However, the excessive inflammation, inevitable infection, downregulated bone remodeling, direct toxicity on macrophages, and diminished vascularity have been exactly elucidated after long-term BPs administration.[37] Target to the pathological features, we fabricate a MgO NPs-encapsulated hydrogel by NHS-functionalized PEG crosslinking with BSA and a-RGD for mandible regeneration. MgO NPs as the nanocomposite component are biodegradable and approved by the FDA and European Medicines Agency (EMA) as medication ingredients.

Developing biomaterials that can replace open surgical procedures with less invasive alternatives is highly demanded especially in maxillofacial plastic surgery.[38] Receiving inspiration from covalent adhesive with NHS-esters, such as CoSeal Surgical Sealant, crosslinking within seconds and have been commonly

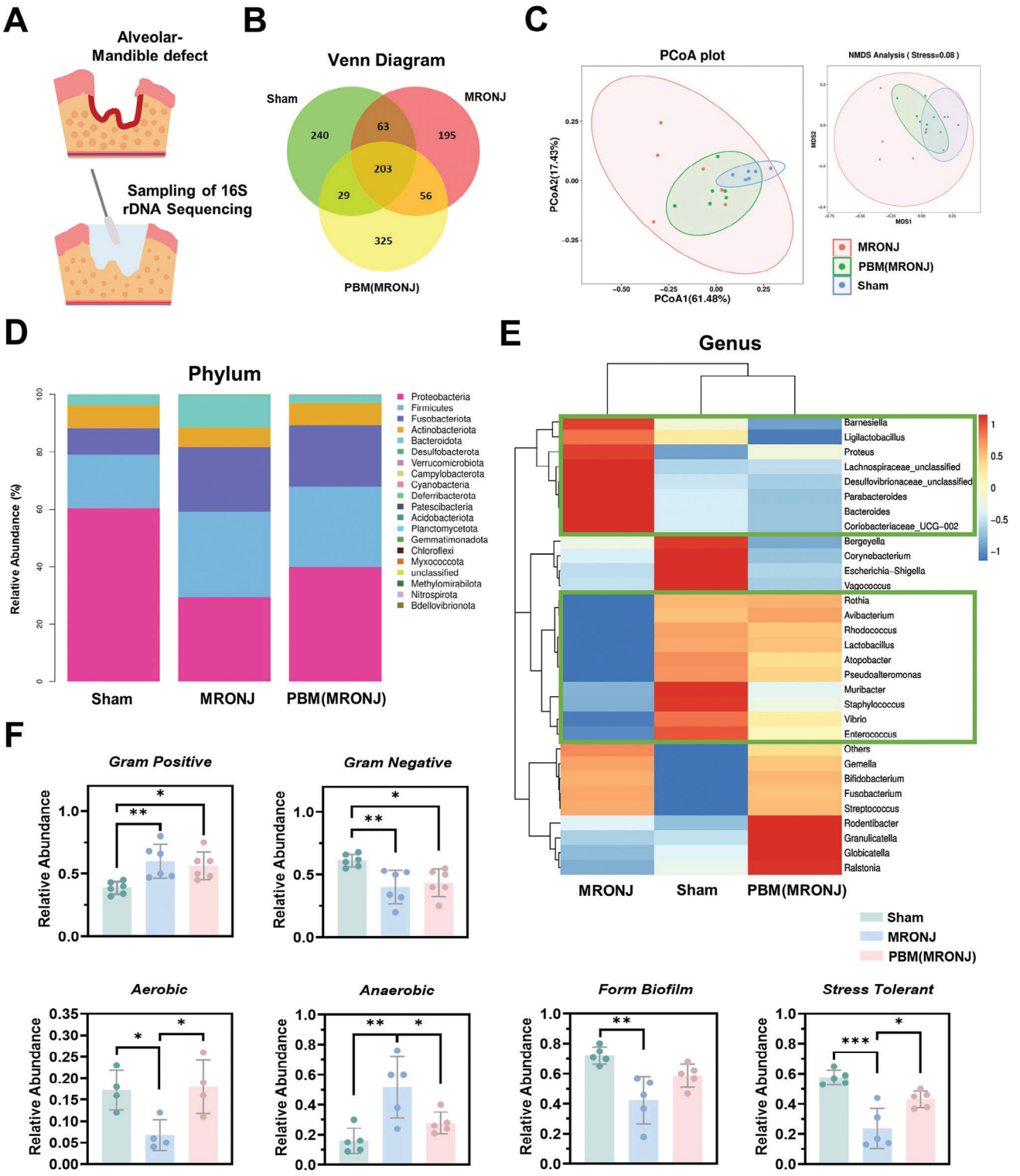

Figure 7. The microbial changes in the defect area following PBM hydrogel treatment. A) Schematic diagram of sampling microbes from the alveolar-mandible defect exposed to the oral cavity. B) Venn diagram of the unique and common amplicon sequence variants (ASVs) identified in different groups. C) PCoA and NMDS plots of the variation in microbial community composition. D) Histogram of species abundance and annotation in phylum level ($n = 6$). E) Heat map of species abundance and annotation in genus level ($n = 6$). F) Bacterial phenotype prediction ($n = 4$-6). *$p < 0.05$, **$p < 0.01$, and ***$p < 0.001$, by one-way ANOVA with Tukey's *post hoc* test.

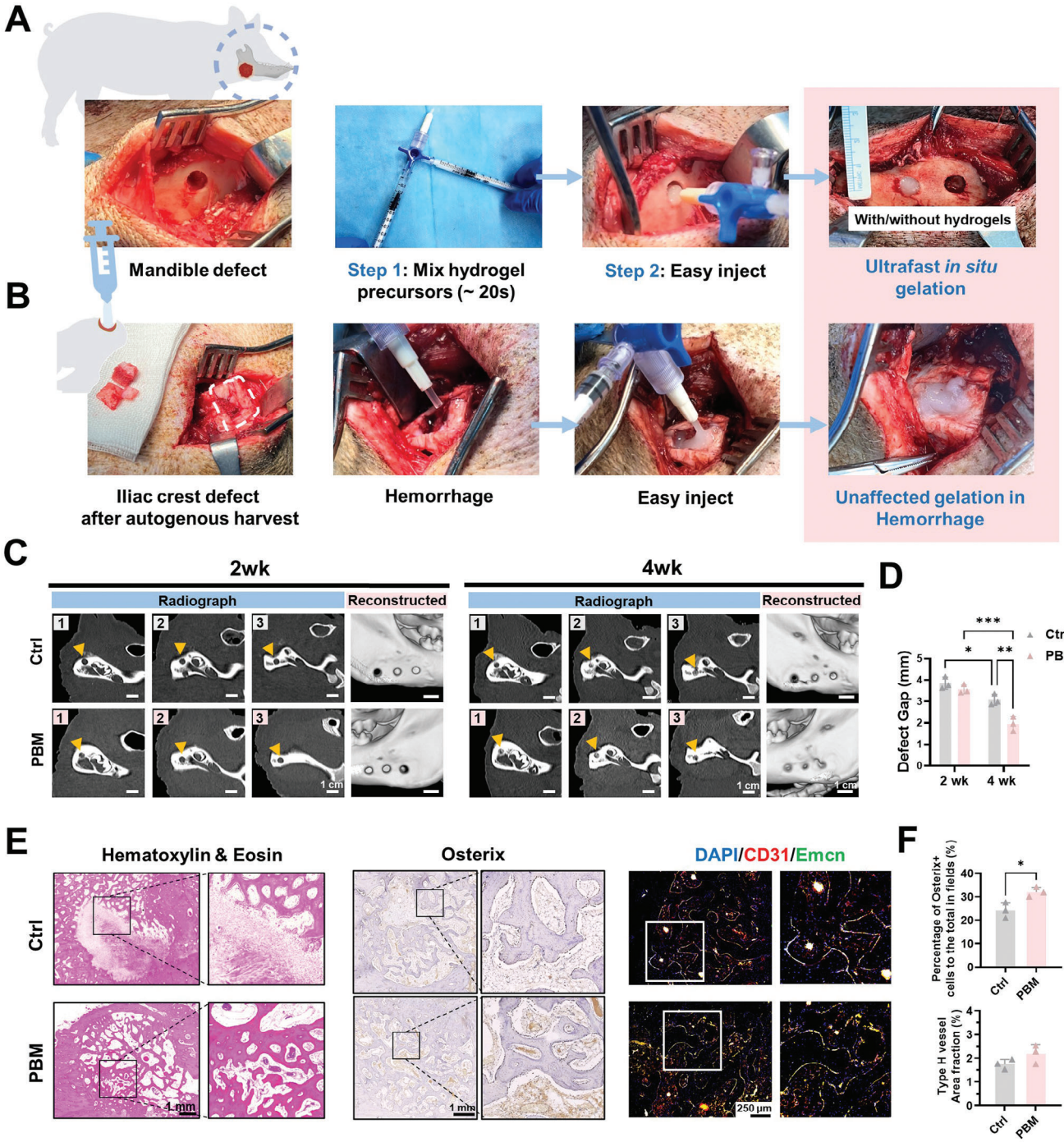

Figure 8. Feasibility and efficacy of PBM hydrogel treatment in mandible and iliac crest defects of minipig. Surgical procedures of the treatment to A) mandible defect and B) iliac crest defects and hydrogel delivery. C) In vivo CT scan and D) quantification of defect gap at 2 and 4 weeks ($n = 3$). E) Representative H&E staining, IHC staining of Osterix, IF staining of Type H vessels in defect sites. F) Quantification of percentage of Osterix+ cells and area fraction of type H vessels in different treatment groups ($n = 3$). *$p < 0.05$, **$p < 0.01$, and ***$p < 0.001$, by two-way ANOVA with Tukey's *post hoc* test (D) and unpaired two-tailed Student's *t*-test (F).

used in hemostats, sealants, and tissue repair.[39] In our study, we utilize 4-arm PEG-NHS to improve the efficiency of integration with bone tissue. By incorporating MgO NPs, the relatively fast gelation rate of hydrogels prevents polymer spillage, facilitating tissue filling within a short time.[40]

MgO NPs not only generate structural diversity but also improve mechanical strength[41] and the bioactive response of hydrogels.[42] The combination of organic-inorganic components is a successful strategy for mimicking the composition and structure of the bone mineral phase including nano-hydroxyapatite

(HA) and type I collagen.[43] Besides, the hydrogel matrix protects MgO NPs from fast reactions with the body fluid leading to an over alkaline environment, achieving sustained Mg^{2+} release in the early healing stage. Mg^{2+} is found to play a crucial role in bone formation and remodeling processes in vivo under certain concentrations.[9a,10b] In our study, we optimize the dose of MgO NPs precisely based on both gelation behaviors and biological activity. We and other groups report that a moderate elevation of Mg^{2+} (5 mM) promotes osteogenic differentiation during the in vitro culture of BMSCs, while a high concentration (>20 mM) has an inhibitory effect.[24] Therefore, PBM(10) hydrogel made by 10 mg mL^{-1} MgO NPs involvement is chosen for the in vivo study, the releasing pattern with ≈1.6 mM Mg^{2+} supplementation per day meets the requirement for the physiological concentration.[44]

Previous studies have provided insights into the crucial role of Mg^{2+} in facilitating interaction between bone and blood vessels.[45] The neural crest-derived mandible is the typical flat bone formed by intramembranous ossification,[46] and relies on angiogenesis for its essential process.[47] The expression of vascular endothelial growth factor in condensing limb bud mesenchyme helps to determine the vascularization of regions surrounding growing prechondrogenic condensations during intramembranous ossification.[48] Type H vessels are recognized within the mandibular condyle and are strongly associated with bone formation.[49] They are crucial for mandible development and regeneration by supporting perivascular osteoprogenitor cells. In the present study, radiological and histological assessments reveal that PBM hydrogel results in superior angiogenesis-osteogenesis coupling bone regeneration characterized by increased functional type H vessels in the defect area. Moreover, PBM hydrogel contributes to combating inflammation, recruiting stem cells, and downregulating keratinization, based on our bulk-RNA sequencing results.

BPs have a direct toxic effect on the oral mucosa, resulting in the invasion of the oral pathogens with subsequent necrosis.[50] Exposed bone is susceptible to infection by abundant bacteria and fungi, where the majority are anaerobes or facultative anaerobes.[51] From our study, 16S rDNA sequencing results reveal a consistent increase in the proportion of anaerobic bacteria in MRONJ. A predominant affiliation to *Firmicutes*, an anaerobic bacterium, is detected in MRONJ patients (71.6%) and patients receiving BPs therapy (70.3%), displaying a significant increase compared to the Ctrl group (59.1%).[33] Remarkably, PBM hydrogel effectively suppresses the elevation of the *Firmicutes* population that occurs under BPs pretreatment. Moreover, PBM hydrogel facilitates the restoration of specific bacterial populations, including *Lactobacillus, Rothia, Atopobacter*, etc. *Lactobacillus* is known for its capacity to adhere to epithelial cells and synthesize antibacterial substances.[52] Notably, *Lactobacillus* demonstrates the appropriate adherence to oral mucosal cells and salivary-coated hydroxyapatite,[53] which potentially protects the exposed oral socket and alveolar bone at the MRONJ site.

Distinct attributes enable our PBM hydrogel to meet the complex and stringent requirements for mandible defects even under the challenging conditions in MRONJ. However, there are also some limitations that should be addressed in future studies. First, the present study focuses on investigating the potential of Mg-nanocomposite hydrogel in combating the systemic factors associated with long-term BPs administration. So, the MRONJ model used in the present study does not involve local dental infection. Further research and design of antibacterial materials are necessary when considering MRONJ cases accompanied by infection. Second, the primary target of BPs has been identified as osteoclasts. It is imperative to explore the potential effects of the developed hydrogel on osteoclast function, which may offer more insights into how hydrogel contributes to the interaction between osteoblast and osteoclast, as well as the bone remodeling and healing process in MRONJ.[54] Moreover, it is worthy to explore the specific cell types directly disrupted after long-term administration of BPs and further investigate if they are the major effectors in PBM-induced regeneration. All such efforts will become a paradigm for pushing the clinical translation of advanced therapies for challenging bone disorders.

4. Experimental Section

General Experimental Approach: The rat experimental protocols conducted in this study were approved by the Animal Experimentation Ethics Committee of the Chinese University of Hong Kong (Approval No. 21-059-CMF). The female Sprague Dawley rats were randomly assigned to different groups while ensuring age-matching. The minipig surgical procedures performed were authorized by the Institutional Animal Care and Use Committee (AMS D2305013P).

Preparation of PBM Hydrogels: PBM hydrogels were synthesized by the amidation reaction. The phosphate-buffered saline (PBS) was used to dissolve different polymers as the precursors A and B. First, 8 wt.% 4 arm-PEG-Succinimidyl Carboxymethyl Ester (4-arm-PEG-NHS, Mw = 10 kDa, ShangHai ToYong Bio-Tech, China) was prepared as precursor A. Second, 2 ug mL^{-1} a-RGD (CGRGDS, GenScript Hong Kong Limited) was added to 10 wt.% BSA (Sigma) solution as solution B, which served as the solvent to mix different concentrations of MgO NPs (Macklin, 50 nm) ranging from 1–30 mg mL^{-1} as precursor B. In the study, PBM(n) hydrogels referred to hydrogels formed with the addition of n mg/mL MgO NPs in precursor B. PBR hydrogels were formed by adjusting the pH of hydrogel precursor B. PBR(pH = m) hydrogels were defined as hydrogels formed under a pH = m condition of hydrogel precursor B. The fabrication of PBR and PBM hydrogels with different gelation times was achieved by thoroughly mixing the 2 precursors (A:B = 1:1, v/v).

Scanning Electron Microscopy: The internal structures of various hydrogels were visualized using scanning electron microscopy (Quanta-400, USA) at an accelerating voltage of 10 kV. To analyze the network distribution and size, the major axis of 10 pores in each sample by ImageJ software (National Institutes of Health, USA) was randomly measured.

Measurement of Gelation Time: The gelation times of hydrogels were determined using the vial tilting method.[55] The prepared precursor hydrogel solutions A and B with different amounts of MgO NPs (1–30 mg mL^{-1}) were quickly added and thoroughly mixed in a vial at room temperature. The gelation time was recorded when there was no flow upon inverting the vial.

As for gelation time in blood, a working concentration of 50 U/ml heparin was added at a ratio of 1:10 to the whole blood to prevent coagulation. 150 µL of precursors A and B were mixed with an equal volume of heparinized whole blood extracted from rats. The gelation time was determined when there was no flow observed upon inverting the vial.

In Vivo Retention of Hydrogel: 5-Aminofluorescein labeled hydrogel precursors (100 µL) were locally injected into SD rats and solidified within seconds. At each set time point, the rats were imaged using an in vivo imaging system (IVIS 200, Xenogen) at the excitation wavelength of 490 nm and emission wavelength of 515 nm to access the retention of PBM hydrogel.

Degradation Behaviors In Vitro: In all tested groups, hydrogels were immersed in 1×PBS solution and incubated in a slow shaker at 37 °C. The

ratio of hydrogel quality to solution volume was 0.1 g mL^{-1} according to ISO 10993 Part 12. The samples were lyophilized overnight and weighed up to 17 days to assess their residual weight. The extracts were collected at different time points, and the concentration of Mg^{2+} in the extracts was measured using inductively coupled plasma-optical emission spectroscopy (ICPE-9820, Shimadzu, Japan) for up to 24 days.

Mechanical Test: The rheological properties of PBR and PBM hydrogels were measured on a rotating rheometer (Kinexus, Lab+, Malvern, UK). For the compression test, the hydrogel samples were compressed at a constant rate of 0.05 mm $^{-1}$s until failure. Strain sweeps were performed at a constant frequency of 1 Hz and a range of 0.1%–100% strain. Frequency sweeps were conducted at a constant shear strain of 0.1% and a frequency range of 0.1–10 Hz.

Cytocompatibility Test In Vitro: Polyethylene glycol diacrylate (PEGDA) hydrogel was prepared as a comparison to PBR and PBM hydrogels. 8 wt.% PEGDA solution was mixed with 0.1 wt.% photoinitiator lithium phenyl-2,4,6-trimethylbenzoylphosphinate (LAP). The solution was sterilized using a 0.22 µm microporous membrane filter, and then exposed to the blue light (10 mW cm^{-2}) for 1 min.

Before mixing with MgO NPs, hydrogel precursor A and solution B were sterilized using a 0.22 µm microporous membrane filter. The hydrogel samples in all groups were fabricated using molds to achieve a diameter of 10 mm and a height of 1 mm and were placed flat at the bottom of a 24-well plate. MMSCs were seeded onto the surface of the hydrogels at a density of 5.0×10^4 cells per well and cultured in 500 µL of αMEM medium in an incubator under standard conditions of 37 °C, 100% relative humidity, and 5% CO_2.

At 1- and 3-days post-implantation, adherent cells in all groups of hydrogels were subjected to live/dead staining using Invitrogen reagents. On day 1, the infiltration distances of the cells in different groups were observed and quantified by confocal microscope (Nikon C2+). On day 3, the percentage of living cells was calculated using ImageJ software.

In Vitro Osteogenic Differentiation: To investigate the osteopromotive effect of hydrogels, MMSC cells were seeded in 24-well plates at a density of 5×10^4 cells per well. The cells were cultured in the osteogenic induction medium (OIM, with 10% FBS, 50 µM ascorbic acid, 10 mM β-glycerophosphate, and 10 nM dexamethasone) supplemented with the extracts of different hydrogel pretreatments. To obtain extracts, hydrogels were immersed in high-glucose DMEM medium (ratio: 0.1 g hydrogel/1 mL medium) and incubated in a slow shaker at 37 °C for 3 days and sterilized using a 0.22 µm microporous membrane filter. Then, replenished the OIM, which was changed every 3 days.

The IF staining for the osteogenesis-related proteins Ocn (Table S1, Supporting Information) in a co-cultured system was conducted based on protocols from the previous study.[56] Proteins in the co-cultured system were visualized via a confocal microscope. Fluorescence intensity normalized to the area was quantified via ImageJ software. ALP activity was measured using the ALP assay Kit (Biosystems). Cell mineralization was investigated by calcium nodule staining using ARS.

Scratch Test: A permanent human cell line (EA.hy926) was used for the scratch test. Seeding EA.hy926 cells in a 12-well culture plate allowed them to grow until they reached confluence. A sterile p200 pipette tip was used to create a straight scratch "wound" across the monolayer cells. Cells will be washed with 1 × PBS to remove any debris or dislodged cells and then replaced by serum-free hydrogel extracts. In this test, hydrogels were immersed in serum-free DMEM medium (ratio: 0.1 g hydrogel /1 mL medium) and incubated in a slow shaker at 37 °C for 3 days and sterilized using a 0.22 µm microporous membrane filter. Cells were cultured in a 37 °C incubator and photographed at 0 and 24 h in the same position. The wound areas in all the tested groups were analyzed using Image J software.

Tube Formation Assay: To investigate the direct angio-promotive effect of hydrogels, tube formation assays were conducted using a published protocol.[57] Specifically, 80 µl of Matrigel (#354 234, Corning) was incubated at 37 °C for 30 min in advance, embedding in a 96-well plate. Next, 2.5×10^4 EA.hy926 cells were seeded onto 96-well plates coated with Matrigel and treated with extracts of various hydrogels without serum for 6 h. Tube formation was observed and quantified using an inverted phase-contrast microscope, and the total branch length and branch number in each group were measured using ImageJ software.

Quantitative Real-Time PCR (qPCR): In this study, qPCR was utilized to evaluate the osteopromotive effects of hydrogels at the transcriptional level. Primer sequences were provided in Table S2 of the Supporting Information. Specifically, the transcription levels of osteogenic genes in MMSCs were assessed. Total mRNA was extracted from the cells using TRIzol (Invitrogen) following the manufacturer's instructions (Takara) and then reverse-transcribed to cDNA using the PrimeScript RT Reagent Kit with gDNA Eraser (Takara). The QuantStudio 7 Pro Real-Time PCR System was employed to determine the transcription levels by RT-qPCR using TB Green Premix Ex Taq (Takara).

For osteogenic gene expression analysis, MMSCs were treated with hydrogel extracts- containing OIM for 5 and 14 days before total RNA extraction. The expression levels of osteogenic genes, *Alp, Osterix*, *Runx2*, *Bmp-2*, and *Ocn*, were normalized to *Gapdh* expression, and the relative expression levels were calculated using the $2^{-\Delta\Delta Ct}$ method.

Animal Surgical Procedure: First, the MRONJ model was established in 12-week-old female SD rats.[58] Each rat received once-weekly intraperitoneal injections of zoledronic acid (0.3 mg k^{-1}g) for continuous 12 weeks. One week after completion of ZOL therapy, animals were anesthetized by injection of a mixture of xylazine, ketamine, and saline. The molars were extracted, and the alveolar bone was destroyed. Then, an extra-oral incision overlying and paralleling the left mandible was made to expose the angle of the mandible, and subcutaneous tissues and masseter muscle were elevated to expose the mandible. A penetrating mandibular defect with a diameter of 3 mm in rats was made around the region of the mandibular body by low-speed dental handpiece and copious saline irrigation. The Sham group without ZOL treatment also underwent the dental procedure and defect creation. In the rat model of MRONJ ($n = 54$ in total), different hydrogels were filled into the mandible defect and then the wound was sutured and closed. Mandible samples were collected at each observation time point to evaluate the therapeutic effects of different hydrogels.

Moreover, 6-month-old Bama miniature pigs were chosen, owing to the similarities in morphology and physiology between minipig and human mandibles.[59] For the surgical procedure in minipig, proper anesthesia was performed by injecting Surital 50 (5 mg k^{-1}g) for muscle anesthesia, followed by maintenance of inhalation anesthesia using isoflurane. A small extra-oral sub-angular incision measuring 5 cm in length was made parallel to the inferior border of the mandible, exposing the lateral portion of the posterior region of the mandibular body. The incision was made through the fascia and muscle, exposing the underlying bone through blunt dissection. The predetermined dimension of the osseous defect was measured and outlined using a ruler and a sterile marker. Then, cylindrical defects with a thickness of 5 mm and a diameter of 6 mm were created by the electric bone drill. The precursor of PBM hydrogel was injected for the experimental group to fill the irregular mandible defect. The same procedure was performed on the contralateral side of the minipig's mandible in the Ctrl group, but no materials were implanted. At specific time points, rats and minipigs were euthanized and tissue at the mandible defect area was collected for radiographic and histological analysis. All the treatment regimens were demonstrated to be safe by referring to the general health conditions of rats and minipigs.

Besides, a skin incision was made along the iliac crest contour in another minipig, followed by dissection through the subcutaneous tissue and muscle layers until the iliac crest was exposed. The dimensions of the donor site were determined and outlined using a sterile marker and a ruler while maintaining a sufficient distance from the anterior superior iliac spine to minimize the risk of stress fractures at the donor site. A sufficient amount of autologous bone flap, measuring 2 cm × 1.5 cm × 2 mm, was carefully dissected medial from the iliac crest using an osteotome with gentle tapping. A raspatory was used to scrape and separate the autologous bone flap from the underlying bone tissue. Next, to evaluate the gelation behavior of PBM hydrogel in the presence of hemorrhage, it was injected dropwise into the donor site. The gelation process was observed and assessed. Subsequently, euthanasia was performed to conclude the experimental procedure.

Micro-CT Analysis: Mandible samples were collected at 4, 8, and 12 weeks for micro-CT analysis using μCT40 (Scanco Medical, Brüttisellen, Switzerland). The acquisition settings were at a voltage of 70 kV and a current of 114 μA to collect images at a resolution of 15 μm per pixel. A low-pass Gaussian filter (Sigma = 1.2, Support = 2, threshold = 200) was selected for microarchitectural 3D reconstruction. Newly-formed bone was evaluated within a conforming volume of interest (VOI), defined as a cylinder in 3 mm diameter and 1.5 mm (100 slides) depth volume in the mandible defect. Microstructural parameters, including BV/TV, BMD, trabecular thickness (Tb.Th), and trabecular number (Tb.N) were then calculated.

Micro-CT Based Angiography: Microfil (Microfil MV-122; Flow Tech, Carver, MA, USA) perfusion was performed at 8 weeks according to the established protocol.[11c,60] The harvested mandibles froze at 4 °C for 24 h and were scanned using a micro-CT (Skyscan1276, Aartselaar, Belgium) after decalcification. The scanning was carried out using acquisition settings (a pixel size of 14.9 μm, an X-ray tube voltage of 80 kVp, and an intensity current of 100 μA), with the entire defect region being scanned. Quantitative analysis was performed on the 200 slides to evaluate the Vessel V/TV, Vessel.N, and Vessel.Th in the defect region.

Histological Analysis: The rat mandibles were collected at 4, 8, and 12 weeks, and major organs including the liver, kidney, lung, heart, and spleen, were dissected at 4 weeks for biosafety validation. All samples were fixed in 4% paraformaldehyde for 2 days and stored in 70% ethanol at 4 °C. The mandible tissues were then decalcified using 9% formic acid at room temperature for 6 days. The minipig mandibles were collected at 8 weeks. The samples were fixed in 4% paraformaldehyde for 3 days and then decalcified using 12.5% Ethylenediaminetetraacetic acid (Sigma) at room temperature for 2 months. All the samples were dehydrated with gradient alcohols and xylene, and then embedded in paraffin for further sectioning. Specifically, mandible tissues were sliced in the coronal position.

Sections were then subjected to H&E staining to visualize the mandible morphology and regeneration status of the mandible defect, as well as potential histopathological changes of metabolic organs. Masson's trichrome staining was performed to indicate the areas of old bone and regenerated bone and highlight collagen deposition or osteoid formation. IHC staining and IF staining were conducted to detect the specific markers that participate in the healing process. The staining procedures were adopted by following the manufacturer's protocols and previously published studies,[61] and observations were made using a microscope (ZEISS AxioPlan2, Germany). For IHC staining, the sections were deparaffinized and rehydrated, followed by quenching of endogenous peroxidase with 3% hydrogen peroxide for 20 min. Then, antigen retrieval was performed to expose the antigenic sites by heating the sections in a 10 mM citrate buffer at a temperature of 65 °C for 30 min. After blocking for 1 h, the samples were incubated overnight at 4 °C with primary antibodies of Osterix and Ocn (Table S1, Supporting Information). Subsequently, slides were washed 3 times by 1×PBST to remove any unbound primary antibody and incubated for 1 h at room temperature with secondary antibody conjugated to horseradish peroxidase (HRP). Finally, the samples were visualized by incubating in DAB (3,3′-diaminobenzidine) (DAB Quanto Chromogen and Substrate, Thermo Fisher Scientific) for 3 min. After counterstaining the tissue sections with a nuclear stain by hematoxylin, the expressions of Osterix and Ocn were observed and quantified (an average of > from slides in each group).

Regarding IF staining, following similar procedures with deparaffination, rehydration, antigen retrieval, and blocking. Then, tissue slides were incubated with primary antibodies of CD31, Ecmn, Osterix, CD105, Postn, Col3a1, and Fn at 4 °C overnight. After rinsing 3 times, tissues were incubated with corresponding secondary antibodies including Alexa Fluor 488, 546, 594, or 647 conjugated anti-rat, anti-mouse, anti-rabbit, or anti-goat antibodies for 1 h at room temperature (Table S1, Supporting Information). Rinsed sections were counterstained with DAPI (Pro-Long Gold antifade reagent, Thermo Fisher Scientific). The expressions of target proteins were observed and quantified in more than 3 slides in each group.

Bulk RNA Sequencing and Analysis: Mandible samples were harvested at 4 weeks for bulk-RNA sequencing, which was performed at BGI (HK) Company Limited. Three regenerated bony tissues within defects were harvested and integrated into one sample to reduce the variability of individuals. Two biological replicates per group were tested and analyzed. Total RNA was isolated using the TRIzol – PureLink hybrid method to have a high yield and purity. The grated samples were incubated in TRIzol for 5 min at room temperature followed by phase separation. RNA purification was performed by adding an equal volume of 70% ethanol made with Diethyl pyrocarbonate (DEPC) water and proceeded to the binding, washing, and elution steps according to the instructions of the Invitrogen PureLink RNA Mini Kit.

Raw sequencing reads were purified by removing low-quality reads, adapter reads, and reads containing contaminated linker or excessive unknown N bases (Trimmomatic). The clean reads were mapped by STAR to the Rattus norvegicus reference genome (mRatBN7.2). Then HTseq software was employed to calculate FPKM values to confirm gene expression. The DEGs were determined using DESeq2 algorithm and *P* values were corrected by the false discovery rate (FDR) algorithm. Screened out DEGs by using the criteria with fold change > 2 and FDR < 0.05. Further, GO enrichment analysis was conducted to elucidate the affected biological processes of the DEGs. The enrichment analysis was performed using the clusterProfiler software. Meanwhile, *P* values were calculated and corrected by FDR. GO terms with *Q* value < 0.05 were considered significantly enriched terms.

16S rDNA Sequencing and Analysis: A total of 18 rats were constructed with alveolar bone defects for 16S rDNA sequencing analysis. The alveolar bone defects were created by grinding ≈2 mm deep from the root of the first and second molar using a low-speed dental handpiece. MRONJ rats were used to investigate the impact of long-term BPs administration on local microorganisms compared to the sham rats. PBM hydrogel was injected and filled into the defects in MRONJ rats. Microorganisms from local alveolar bone defects were sampled at 2 weeks using oral swabs for 16S rDNA sequencing, which was performed at Biotree Biomedical Technology Company Limited. The 16S rDNA libraries were sequenced on the NovaSeq PE250 platform. Samples were sequenced on an Illumina NovaSeq platform. Quality filtering on the raw reads was performed under specific filtering conditions to obtain high-quality clean tags according to the fqtrim (v0.94). Chimeric sequences were filtered using Vsearch software (v2.3.4). Following this, dereplication was carried out using DADA2, resulting in the generation of a feature table and feature sequences. Then according to the SILVA (release 138) classifier, feature abundance was normalized using the relative abundance of each sample. Diagrams were implemented using the R package (v3.5.2).

Statistical Analysis: The data were analyzed using GraphPad Prism software version 8 (GraphPad Software Inc.). Mann-Whitney *U* test and unpaired two-tailed Student's *t*-test were used for comparison between 2 groups. One-way ANOVA followed by Tukey's *post hoc* test was used for the comparison of more than 2 groups with one factor. Two-way ANOVA followed by Tukey's *post hoc* test was used for the analysis of data with 2 factors. $p < 0.05$ was considered to be statistically significant.

Supporting Information

Supporting Information is available from the Wiley Online Library or from the author.

Acknowledgements

The authors would like to thank the support from Areas of Excellence (AoE/M-402/20), and General Research Fund (14109421) from the Research Grants Council of Hong Kong, Natural Science Foundation of Guangdong Province (2021A1515011204), Direct grants (2020.058 and 2020.060) from the Chinese University of Hong Kong, Mainland-Hong Kong Joint Funding Scheme (MHP/030/20) from Innovation and Technology Commission of Hong Kong. Besides, the authors especially appreciated the support from Mr. Chui Ying Yip from the University of Hong Kong for his assistance in micro-CT-based angiography. Moreover, the authors would like to extend our sincere thanks to the staff of Shenzhen Advanced

Medical Service Co., Ltd for their expertise and assistance in conducting the minipig experiments and sample collections.

Conflict of Interest

The authors declare no conflict of interest.

Author Contributions

J.G., H.Y., and L.C. contributed equally to this work. J.G., L.Q., and J.X. conceived this project. J.G. designed and fabricated the innovative hydrogels. J.G., H.Y., and L.C. performed in vitro and in vivo experiments. L.C. performed in silico bioinformatic analysis. J.G., H.Y., Y.Z., and J.X. conducted the large animal surgery. J.G., H.Y., and L.C. collected and analyzed the data. W.Z., Y.Z., X.L., B.Y., B.D., X.C., L.L., Z.C., Y.L., L.Z., W.L., and W.T. assisted with the experiments and characterizations. J.G. wrote the manuscript. L.Q. and J.X. supervised the project and revised the manuscript.

Data Availability Statement

The data that support the findings of this study are available on request from the corresponding author. The data are not publicly available due to privacy or ethical restrictions.

Keywords

bone regeneration, hydrogel, magnesium, nanoparticle, osteonecrosis

Received: November 29, 2023
Revised: September 27, 2024
Published online: October 10, 2024

[1] Y. Li, S.-K. Chen, L. Li, L. Qin, X.-L. Wang, Y.-X. Lai, *J. Orthopaed. Translat.* **2015**, *3*, 95.
[2] a) M. Kos, *Arch. Med. Sci.* **2015**, *11*, 319; b) M. Ishimaru, S. Ono, K. Morita, H. Matsui, Y. Hagiwara, H. Yasunaga, *J. Oral Maxillofacial Surg.* **2022**, *80*, 714.
[3] S. Cremers, M. T. Drake, F. H. Ebetino, J. P. Bilezikian, R. G. G. Russell, *Br. J. Clin. Pharmacol.* **2019**, *85*, 1052.
[4] T. H. Kim, W. G. Seo, C. H. Koo, J. H. Lee, *J. Korean Assoc. Oral Maxillofac Surg.* **2016**, *42*, 193.
[5] a) K. Rupel, G. Ottaviani, M. Gobbo, L. Contardo, G. Tirelli, P. Vescovi, R. Di Lenarda, M. Biasotto, *Oral Oncol.* **2014**, *50*, 1049; b) D. Sharma, S. Ivanovski, M. Slevin, S. Hamlet, T. S. Pop, K. Brinzaniuc, E. B. Petcu, R. I. Miroiu, *Vascular Cell* **2013**, *5*, 1.
[6] A. Fouda, A. M. Eid, M. A. Abdel-Rahman, E. F. El-Belely, M. A. Awad, S. E. Hassan, Z. E. Al-Faifi, M. F. Hamza, *Front. Bioeng. Biotechnol.* **2022**, *10*, 849921.
[7] S. Banai, L. Haggroth, S. E. Epstein, W. Casscells, *Circ. Res.* **1990**, *67*, 645.
[8] W. Qiao, K. H. M. Wong, J. Shen, W. Wang, J. Wu, J. Li, Z. Lin, Z. Chen, J. P. Matinlinna, Y. Zheng, S. Wu, X. Liu, K. P. Lai, Z. Chen, Y. W. Lam, K. M. C. Cheung, K. W. K. Yeung, *Nat. Commun.* **2021**, *12*, 2885.
[9] a) H. S. Han, I. Jun, H. K. Seok, K. S. Lee, K. Lee, F. Witte, D. Mantovani, Y. C. Kim, S. Glyn-Jones, J. R. Edwards, *Adv. Sci.* **2020**, *7*, 2000800; b) E. Baldoli, J. A. Maier, *Angiogenesis* **2012**, *15*, 47.
[10] a) Y. Yang, X. Xiong, J. Chen, X. Peng, D. Chen, F. Pan, *J. Magnes. Alloys* **2021**, *9*, 705; b) J. L. Wang, J. K. Xu, C. Hopkins, D. H. K. Chow, L. Qin, *Adv. Sci.* **2020**, *7*, 1902443.
[11] a) D. M. Black, E. J. Geiger, R. Eastell, E. Vittinghoff, B. H. Li, D. S. Ryan, R. M. Dell, A. L. Adams, *N. Engl. J. Med.* **2020**, *383*, 743; b) N. Zheng, J. Xu, Y. C. Ruan, L. Chang, X. Wang, H. Yao, J. Wang, R. Zhang, Q. Xue, N. Tang, T. Ong, J. Schilcher, R. J. O'Keefe, L. Qin, *Mater. Today* **2022**, *52*, 43; c) W. Zhu, J. Guo, W. Yang, Z. Tao, X. Lan, L. Wang, J. Xu, L. Qin, Y. Su, *J. Orthopaed. Translat.* **2022**, *33*, 153.
[12] a) X. Li, B. Dai, J. Guo, Y. Zhu, J. Xu, S. Xu, Z. Yao, L. Chang, Y. Li, X. He, D. H. K. Chow, S. Zhang, H. Yao, W. Tong, T. Ngai, L. Qin, *ACS Nano* **2022**, *16*, 18071; b) H. Zhou, B. Liang, H. Jiang, Z. Deng, K. Yu, *J. Magnes. Alloys* **2021**, *9*, 779.
[13] N. T. Nguyen, N. Grelling, C. L. Wetteland, R. Rosario, H. Liu, *Sci. Rep.* **2018**, *8*, 16260.
[14] M. Kos, *Archives of Medical Science*, AMS, **2015**, *11*, 319.
[15] a) A. Chen, S. Deng, J. Lai, J. Li, W. Chen, S. N. Varma, J. Zhang, C. Lei, C. Liu, L. Huang, *Molecules* **2023**, 28; b) J. Guo, H. Yao, X. Li, L. Chang, Z. Wang, W. Zhu, Y. Su, L. Qin, J. Xu, *Bioact. Mater.* **2023**, *21*, 175.
[16] W. Huang, S. Cheng, X. Wang, Y. Zhang, L. Chen, L. Zhang, *Adv. Funct. Mater.* **2021**, *31*, 2009189.
[17] a) H. Tan, D. Jin, J. Sun, J. Song, Y. Lu, M. Yin, X. Chen, X. Qu, C. Liu, *Bioact. Mater.* **2021**, *6*, 905; b) F. Li, V. X. Truong, P. Fisch, C. Levinson, V. Glattauer, M. Zenobi-Wong, H. Thissen, J. S. Forsythe, J. E. Frith, *Acta Biomater.* **2018**, *77*, 48.
[18] a) S. S. Banerjee, N. Aher, R. Patil, J. Khandare, *J. Drug Deliv.* **2012**, *2012*, 1; b) D. F. Quevedo, N. Habibi, J. V. Gregory, Y. Hernandez, T. D. Brown, R. Miki, B. N. Plummer, S. Rahmani, J. E. Raymond, S. Mitragotri, J. Lahann, *Macromol. Rapid Commun.* **2020**, *41*, 2000425.
[19] J. Ma, M. Thompson, N. Zhao, D. Zhu, *J. Orthopaed. Translat.* **2014**, *2*, 118.
[20] J. MarieáVasquez, *Polym. Chem.* **2017**, *8*, 1283.
[21] Y. Gao, K. Peng, S. Mitragotri, *Adv. Mater.* **2021**, *33*, 2006362.
[22] R. Dimatteo, N. J. Darling, T. Segura, *Adv. Drug Delivery Rev.* **2018**, *127*, 167.
[23] D. J. Lee, J. Kwon, L. Current, K. Yoon, R. Zalal, X. Hu, P. Xue, C.-C. Ko, *J. Tissue Engineer.* **2019**, *10*, 204173141983042.
[24] S. Lin, G. Yang, F. Jiang, M. Zhou, S. Yin, Y. Tang, T. Tang, Z. Zhang, W. Zhang, X. Jiang, *Adv. Sci.* **2019**, *6*, 1900209.
[25] a) M. Biasotto, S. Chiandussi, S. Zacchigna, S. Moimas, F. Dore, G. Pozzato, F. Cavalli, F. Zanconati, L. Contardo, M. Giacca, R. Di Lenarda, *J. Oral Pathol. Med.* **2010**, *39*, 390; b) K. L. Marino, I. Zakhary, R. A. Abdelsayed, J. A. Carter, J. C. O'Neill, R. M. Khashaba, M. Elsalanty, M. R. Stevens, J. L. Borke, *J. Oral Implantol.* **2012**, *38*, 511.
[26] W. Y. Zhu, W. F. Yang, L. Wang, X. Lan, Z. Y. Tao, J. Guo, J. Xu, L. Qin, Y. X. Su, *J. Orthopaed. Translat.* **2023**, *39*, 55.
[27] A. P. Kusumbe, S. K. Ramasamy, R. H. Adams, *Nature* **2014**, *507*, 323.
[28] S. Abtahi, X. Chen, S. Shahabi, N. Nasiri, *ACS Mater. Au* **2023**, *3*, 394.
[29] a) X. Shen, Y. Zhang, Y. Gu, Y. Xu, Y. Liu, B. Li, L. Chen, *Biomaterials* **2016**, *106*, 205; b) P. Chen, J. Tao, S. Zhu, Y. Cai, Q. Mao, D. Yu, J. Dai, H. Ouyang, *Biomaterials* **2015**, *39*, 114.
[30] L. He, X. Sun, Z. Liu, Y. Qiu, Y. Niu, *Int. J. Oral Sci.* **2020**, *12*, 30.
[31] M. Martínez, T. T. Postolache, B. García-Bueno, J. C. Leza, E. Figuero, C. A. Lowry, S. Malan-Müller, *Front. Psychiatry.* **2021**, *12*, 814177.
[32] a) D. K. Meyer, A. Reboli, *Principles Pract. Infect. Dis.* **2014**, *2*, 2695; b) C. Badet, N. B. Thebaud, *Open Microbiol. J.* **2008**, *2*, 38.
[33] S. Pushalkar, X. Li, Z. Kurago, L. V. Ramanathapuram, S. Matsumura, K. E. Fleisher, R. Glickman, W. Yan, Y. Li, D. Saxena, *Int. J. Oral Sci.* **2014**, *6*, 219.
[34] G. Campisi, O. Di Fede, A. Musciotto, A. Lo Casto, L. Lo Muzio, F. Fulfaro, G. Badalamenti, A. Russo, N. Gebbia, *Ann. Oncol.* **2007**, *18*, vi168.
[35] a) M. Ulmner, F. Jarnbring, *J. Oral Maxillofac. Surg.* **2014**, *72*, 76; b) J. Coello-Suanzes, V. Rollon-Ugalde, A. Castaño-Seiquer, E. Lledo-Villar, J. Herce-Lopez, P. Infante-Cossio, A. Rollon-Mayordomo, *J. Oral Dis.* **2018**, *24*, 1029.

[36] S. L. Ruggiero, T. B. Dodson, J. Fantasia, R. Goodday, T. Aghaloo, B. Mehrotra, F. O'Ryan, American Association of Oral and Maxillofacial Surgeons, *J. Oral Maxillofac. Surg.* **2014**, *72*, 1938.
[37] a) P. Vestergaard, K. Schwartz, L. Rejnmark, L. Mosekilde, E. M. Pinholt, *J. Oral Maxillofac. Surg.* **2012**, *70*, 821; b) D. Zhao, D. Xiao, M. Liu, J. Li, S. Peng, Q. He, Y. Sun, J. Xiao, Y. Lin, *Int. J. Oral Sci.* **2022**, *14*, 23.
[38] a) T. Birman, D. Seliktar, *Adv. Funct. Mater.* **2021**, *31*, 2100628; b) M. G. Raucci, U. D'Amora, A. Ronca, L. Ambrosio, *Adv. Healthcare Mater.* **2020**, *9*, 2000349.
[39] K. E. Rodgers, F. G. Burleson, G. R. Burleson, M. J. Wolfsegger, K. M. Lewis, H. Redl, *Am. J. Obstet. Gynecol.* **2010**, *203*, 494e1.
[40] P. J. Bouten, M. Zonjee, J. Bender, S. T. Yauw, H. van Goor, J. C. van Hest, R. Hoogenboom, *Prog. Polym. Sci.* **2014**, *39*, 1375.
[41] Y. Chen, C. Li, Z. Wang, J. Long, R. Wang, J. Zhao, W. Tang, Y. Zhao, L. Qin, S. Peng,, Y. Lai, *Appl. Mater. Today.* **2021**, *25*, 101182.
[42] P. Thoniyot, M. J. Tan, A. A. Karim, D. J. Young, X. J. Loh, *Adv. Sci.* **2015**, *2*, 1400010.
[43] X. Liu, Y. Wu, X. Zhao, Z. Wang, *Carbohydr. Polym.* **2021**, *267*, 118179.
[44] J. H. De Baaij, J. G. Hoenderop, R. J. Bindels, *Physiol. Rev.* **2015**, *95*, 1.
[45] a) Y. Xu, C. Xu, L. He, J. Zhou, T. Chen, L. Ouyang, X. Guo, Y. Qu, Z. Luo, D. Duan, *Bioact. Mater.* **2022**, *16*, 271; b) H. Cao, L. Li, L. Li, X. Meng, Y. Liu, W. Cheng, P. Zhang, Y. Gao, L. Qin, X. Wang, *J. Orthop. Translat.* **2022**, *36*, 52.
[46] X. Ye, J. He, S. Wang, Q. Han, D. You, B. Feng, F. Zhao, J. Yin, M. Yu, H. Wang, H. Yang, *Int. J. Oral Sci.* **2022**, *14*, 31.
[47] a) H. Yao, J. Guo, W. Zhu, Y. Su, W. Tong, L. Zheng, L. Chang, X. Wang, Y. Lai, L. Qin, J. Xu, **2022**, *14*, 2397; b) Y. Q. Yang, Y. Y. Tan, R. Wong, A. Wenden, L. K. Zhang, A. B. Rabie, *Int. J. Oral Sci.* **2012**, *4*, 64.
[48] a) I. Eshkar-Oren, S. V. Viukov, S. Salameh, S. Krief, C. Oh, H. Akiyama, H.-P. Gerber, N. Ferrara, E. Zelzer, **2009**; b) H. Yao, J. Guo, W. Zhu, Y. Su, W. Tong, L. Zheng, L. Chang, X. Wang, Y. Lai, L. Qin, J. Xu, *Pharmaceutics* **2022**, 14.
[49] H. Li, L. Liao, Y. Hu, Y. Xu, Y. Zhang, F. Huo, W. Tian, W. Guo, *J. Dental Res.* **2021**, *100*, 983.
[50] K. Anavi-Lev, Y. Anavi, G. Chaushu, D. M. Alon, G. Gal, I. J. O. s. Kaplan, *Radiology* **2013**, *115*, 660.
[51] J. Jakiel, M. Rahnama, J. Szczerba-Gwóźdź, *Contemp. Oncol.* **2016**, *20*, 486.
[52] H. S. Na, S. Y. Kim, H. Han, H.-J. Kim, J.-Y. Lee, J.-H. Lee, J. Chung, *J. Clin. Med.* **2020**, *9*, 1549.
[53] A. Etebarian, T. Sheshpari, K. Kabir, H. Sadeghi, A. Moradi, A. J. C. Hafedi, Clin. Exp. Dent. Res. Research, **2023**, *9*, 746.
[54] a) D. Nogueira, I. M. Caldas, R. J. Dinis-Oliveira, *Arch. Oral Biol.* **2023**, *155*, 105792; b) M. J. Rogers, J. Mönkkönen, M. A. Munoz, *Bone* **2020**, *139*, 115493; c) L. L. Chang, R. Eastell, P. D. Miller, *N. Engl. J. Med.* **2022**, *386*, 1467.
[55] a) R. Zhong, Q. Tang, S. Wang, H. Zhang, F. Zhang, M. Xiao, T. Man, X. Qu, L. Li, W. Zhang, H. Pei, *Adv. Mater.* **2018**, *30*, 1706887; b) J. Tropp, C. P. Collins, X. Xie, R. E. Daso, A. S. Mehta, S. P. Patel, M. M. Reddy, S. E. Levin, C. Sun, J. Rivnay, *Adv. Mater.* **2023**, 2306691.
[56] R. Li, S. Lin, M. Zhu, Y. Deng, X. Chen, K. Wei, J. Xu, G. Li, L. Bian, *Sci. Adv.* **2019**, *5*, eaaw3896.
[57] P. Gao, B. Fan, X. Yu, W. Liu, J. Wu, L. Shi, D. Yang, L. Tan, P. Wan, Y. Hao, S. Li, W. Hou, K. Yang, X. Li, Z. Guo, *Bioact. Mater.* **2020**, *5*, 680.
[58] a) D. Sharma, S. Hamlet, E. Petcu, S. Ivanovski, *Oral Dis.* **2013**, *19*, 747; b) W. Y. Zhu, J. Guo, W. F. Yang, Z. Y. Tao, X. Lan, L. Wang, J. Xu, L. Qin, Y. X. Su, *J. Orthopaed. Translat.* **2022**, *33*, 153.
[59] B. van Oirschot, E. J. W. Geven, A. G. Mikos, J. van den Beucken, J. A. Jansen, *Tissue Engineering. Part C, Methods* **2022**, *28*, 193.
[60] a) L. Zheng, H. Cao, S. Chen, T. Tang, W. Fu, L. Huang, D. H. K. Chow, Y. Wang, J. F. Griffith, W. He, *J. Bone Miner. Res.* **2015**, *30*, 2044; b) Y. Li, J. Xu, J. Mi, X. He, Q. Pan, L. Zheng, H. Zu, Z. Chen, B. Dai, X. Li, *Biomaterials* **2021**, *275*, 120984.
[61] a) Y. Zhang, J. Xu, Y. C. Ruan, M. K. Yu, M. O'Laughlin, H. Wise, D. Chen, L. Tian, D. Shi, J. Wang, S. Chen, J. Q. Feng, D. H. Chow, X. Xie, L. Zheng, L. Huang, S. Huang, K. Leung, N. Lu, L. Zhao, H. Li, D. Zhao, X. Guo, K. Chan, F. Witte, H. C. Chan, Y. Zheng, L. Qin, *Nat. Med.* **2016**, *22*, 1160; b) H. Yao, J. Xu, J. Wang, Y. Zhang, N. Zheng, J. Yue, J. Mi, L. Zheng, B. Dai, W. Huang, S. Yung, P. Hu, Y. Ruan, Q. Xue, K. Ho, L. Qin, *Bioact. Mater.* **2021**, *6*, 1341.